Ultra Reliable Detection of Imminent Collision for Enhanced Occupant Safety

Final Report

Prepared by:

Saber Taghvaeeyan
Zhen Sun
Michael Mott
Rajesh Rajamani

Department of Mechanical Engineering
University of Minnesota

CTS 12-07

Technical Report Documentation Page

1. Report No.	2.	3. Recipients Accession No.	
CTS 12-07			
4. Title and Subtitle Ultra Reliable Detection of Imminent Collision for Enhanced Occupant Safety		5. Report Date May 2012 6.	
7. Author(s) Saber Taghvaeeyan, Zhen Sun, Michael Mott and Rajesh Rajamani		8. Performing Organization Report No.	
9. Performing Organization Name and Address Department of Mechanical Engineering University of Minnesota 111 Church Street SE Minneapolis, MN 55455		10. Project/Task/Work Unit No. CTS Project #2010035 11. Contract (C) or Grant (G) No.	
12. Sponsoring Organization Name and Address Intelligent Transportation Systems Institute Center for Transportation Studies University of Minnesota 200 Transportation and Safety Building 511 Washington Ave. SE Minneapolis, MN 55455		13. Type of Report and Period Covered Final Report 14. Sponsoring Agency Code	
15. Supplementary Notes http://www.its.umn.edu/Publications/ResearchReports/			

16. Abstract (Limit: 250 words)

This project focuses on the use of anisotropic magnetoresisitve (AMR) sensors for detection of an imminent unavoidable collision. An analytical formulation is developed for the variation of the magnetic field around a car as a function of position. Based on magnetic field measurements using AMR sensors, the position and velocity of any other car can be estimated and an imminent collision detected just prior to collision. The developed AMR sensor system has very high refresh rates, works at very small distances down to zero meters and is highly inexpensive. A variety of experimental results are presented to demonstrate the performance of the system for both one-dimensional and two-dimensional relative motion between cars. The second part of the project conducts simulations to show the benefits of detecting an imminent collision using the developed AMR sensors. An occupant model is developed to analyze occupant motion inside a car during a frontal collision. Analytical formulations and simulations are used to show how occupant safety can be enhanced when knowledge of an imminent collision is available.

17. Document Analysis/Descriptors	18. Availability Statement		
Collision detection, Collision sensors, Occupant safety, Collision avoidance systems, Automatic crash notification, Sensors, Electromagnetic fields, Crash victim simulation, Vehicle safety	No restrictions. Document available from: National Technical Information Services, Alexandria, Virginia 22312		
19. Security Class (this report) Unclassified	20. Security Class (this page) Unclassified	21. No. of Pages 93	22. Price

Ultra Reliable Detection of Imminent Collision for Enhanced Occupant Safety

Final Report

Prepared by:

Saber Taghvaeeyan
Zhen Sun
Michael Mott
Rajesh Rajamani

Department of Mechanical Engineering
University of Minnesota

May 2012

Published by:

Intelligent Transportation Systems Institute
Center for Transportation Studies
University of Minnesota
200 Transportation and Safety Building
511 Washington Avenue SE
Minneapolis, Minnesota 55455

Acknowledgments

The authors wish to acknowledge those who made this research possible. The study was funded by the Intelligent Transportation Systems (ITS) Institute, a program of the University of Minnesota's Center for Transportation Studies (CTS). Financial support was provided by the United States Department of Transportation's Research and Innovative Technologies Administration (RITA).

Table of Contents

List of Figures

List of Tables

Executive Summary

This project focuses on the use of anisotropic magnetoresistive (AMR) sensors for imminent crash detection in cars. The AMR sensors are used to measure the magnetic field from another vehicle in close proximity, so as to estimate relative position, velocity and orientation of the vehicle from the measurement.

An analytical formulation is first developed for the relationship between magnetic field and vehicle position for one-dimensional motion. A first order inverse relationship between magnetic field and vehicle position is predicted. This relationship can be used for detection of imminent frontal and rear-end collisions. However, the challenge in the use of the relationship comes from the fact that the parameters in the relationship vary with each type of car. The type of vehicle encountered is not known apriori. An adaptive filter based on the extended Kalman filter (EKF) is therefore developed to automatically tune filter parameters for each encountered car and reliably estimate relative car position. The utilization of an additional sonar sensor during the initial detection of the encountered vehicle is shown to highly speed up the parameter convergence of the filter. Experimental results are presented from a large number of tests with various vehicles to show that the proposed sensor system is viable and can accurately estimate one-dimensional position with a 2-cm accuracy in the 0-3 meters range.

Next, an analytical formulation for the planar variation of the magnetic field from a car is developed for two-dimensional position and orientation estimation. The use of both sonar and AMR sensors is shown to lead to a simple estimator in which the angular position of the target car can be estimated purely from the sonar sensors. The radial distance and the orientation of the car are then obtained from the AMR sensors. Experimental results are presented for both a laboratory wheeled car door and for a full scale passenger sedan. Experimental results for the passenger sedan show that planar position, relative angular position and orientation can be accurately estimated for relative motion at different oblique angles.

The final part of the project focuses on occupant dynamics during a front-to-back collision and the use of predictive collision information to enhance occupant safety. Occupant dynamics are modeled using a Lagrangian formulation with three degrees of freedom that consist of pelvis translation, torso rotation and head/neck rotation. A control law is developed for the forces from lap and shoulder seat belts. Predictive information in which an imminent collision is known just 100 milli-seconds before it occurs is shown to provide significant benefits. A control law that utilizes predictive information can provide significantly enhanced occupant safety compared to regular seat belts and seat-belts that utilize only pre-tightening.

The contributions of this project are the development of a novel vehicle position estimation and imminent crash detection system, experimental validation of the developed sensor system and preliminary demonstration through simulations of the value of the developed system in enhancing occupant safety.

1 Analysis of Vehicle Magnetic Signatures Using AMR Sensors

This chapter analyzes the magnetic signatures of cars and develops an analytical relationship between position and magnetic field for one-dimensional motion of a car.

1.1 Introduction

Recently there has been significant interest in the use of magnetoresisitve devices to analyze magnetic signatures for useful sensor applications in a number of domains. Biomagnetic signatures of the electrical activity of the human heart have been recorded using giant magnetoreisitive (GMR) sensors [1]. A self-powered magnetoresisitive sensor capable of detecting dc and ac external magnetic fields in the thermal noise regime has been developed [2]. A magnetoresisitive device incorporating microfluidic channels has been developed to detect magnetic beads and measure their flowspeeds in a cytometer [3]. A magnetoresisitive chip has been used for detection of resonance in microcantilevers [4]. Tunneling magnetoresisitive sensors have also been used for high resolution particle detection [5].

The use of anisotropic magnetoresisitive (AMR) sensors to detect the change in magnetic field induced by a passing vehicle has been used to measure the traffic flow rate on a road [6], [7]. However, the magnetic field from a vehicle has never been analyzed to evaluate if the size of vehicle, distance from vehicle and relative velocity can be estimated from it. This chapter focuses on analyzing the magnetic field from a vehicle as a function of its position in order to estimate vehicle position from measured magnetic field.

The advantage of estimating position from a vehicle's magnetic field is that this type of position measurement would work at very small inter-vehicle distances on roads. Currently radar and laser sensors are used on some luxury cars to measure distances to other vehicles [14, 15, 16, 17, 18]. However, such sensors cannot measure distance at close inter-vehicle spacing (< 1 m). Furthermore, they are very expensive sensors – for example, a radar distance measuring unit can cost as much as $2000. On the other hand, the AMR sensors for measurement of magnetic field proposed in this project cost less than $10 each. Hence such sensors can be spread all around the vehicle body. Since they work at very small inter-vehicle distances, they can be used to detect an imminent collision and its severity just before the collision occurs (a few tens of milli-seconds before the crash occurs).

The development of such imminent collision detection systems will lead to smart deployment systems for seat belts and airbags, providing improved safety for passengers during a crash. Such crash detection systems can also be used in technologies that actively enhance vehicle crush space to mitigate the effects of the crash. For such applications (where airbags can be triggered based on collision warnings), a far more fool-proof and close-range collision detection system is needed that cannot be provided by long range radar or laser sensors.

For such collision detection, a sensor system that is inexpensive, continues to work at very close range values, has a wide field of view at short range and measures the other car's position and velocity just before collision is required. Such a sensor system can be obtained from magnetoresistive devices that measure magnetic field.

1.2 Analysis of Vehicle Magnetic Signatures

An analytical expression is developed for the magnetic field along the z axis around a rectangular block of magnetic material, as shown in Figure 1.1.

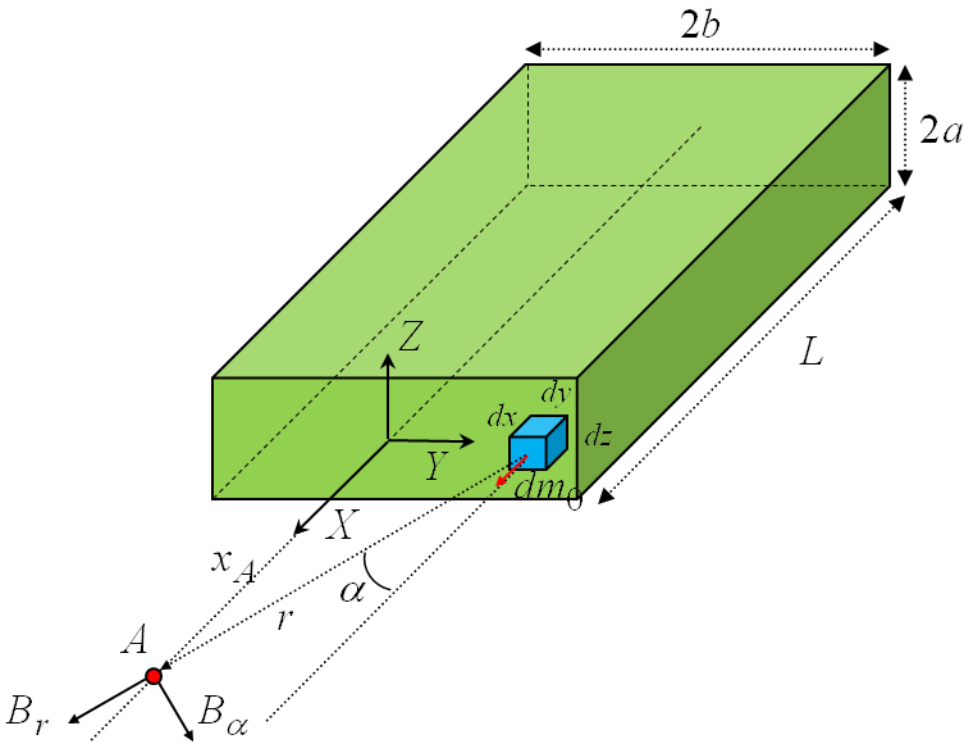

Figure 1.1. Analysis of magnetic field around a rectangular block

According to [9], the planar components of the magnetic field generated by the element $\boldsymbol{dm_0}$ at the point A are given by

$$B_r = \frac{\mu_0 dm_0}{2\pi r^3}\cos\alpha \tag{1.1}$$

$$B_\alpha = \frac{\mu_0 dm_0}{4\pi r^3}\sin\alpha \tag{1.2}$$

Hence, the magnetic field generated by $\boldsymbol{dm_0}$ along z axis would be equal to

$$B_z = B_r cos\alpha - B_\alpha sin\alpha \tag{1.3}$$

or

$$B_z = \frac{\mu_0 dm_0}{4\pi r^3}(2\cos^2\alpha - \sin^2\alpha) \tag{1.4}$$

The magnetic field generated by the front surface of the block can be obtained from the following integral

$$B_{z-fs} = \int_{-a}^{a}\int_{-b}^{b} \frac{\mu_0 m_0}{4\pi r^3}(2\cos^2\alpha - \sin^2\alpha)dxdy \tag{1.5}$$

Express r and α in terms of x and y. Also, assuming that point A is at distance d from the surface, we have

$$r^2 = x^2 + y^2 + d^2$$

$$\alpha = \text{atan}\left(\frac{\sqrt{x^2+y^2}}{d}\right) \rightarrow \quad \sin\alpha = \frac{\sqrt{x^2+y^2}}{\sqrt{x^2+y^2+d^2}} \ , \quad \cos\alpha = \frac{d}{\sqrt{x^2+y^2+d^2}}$$

Hence equation (5) can be rewritten as

$$B_{z-fs} = \frac{\mu_0 m_0}{4\pi}\int_{-a}^{a}\int_{-b}^{b} \frac{2d^2 - (x^2+y^2)}{(d^2+x^2+y^2)^{5/2}}dxdy \tag{1.6}$$

Using MATLAB and "int" command in the Symbolic toolbox the result of the above integration will be

$$B_{z-fs} = \frac{\mu_0 m_0}{\pi}\frac{ab(2d^2 + 3d^2a^2 + 3d^2b^2 + a^4 + 2a^2b^2 + b^4)}{(d^2+a^2)(d^2+b^2)(d^2+a^2+b^2)^{3/2}}$$

which can be further simplified as follows

$$B_{z-fs} = \frac{\mu_0 m_0}{\pi} \frac{ab(2d^2 + a^2 + b^2)(d^2 + a^2 + b^2)}{(d^2 + a^2)(d^2 + b^2)(d^2 + a^2 + b^2)^{3/2}}$$
$$= \frac{\mu_0 m_0}{\pi} \frac{ab(2d^2 + a^2 + b^2)}{(d^2 + a^2)(d^2 + b^2)(d^2 + a^2 + b^2)^{1/2}} \quad (1.7)$$

To obtain the magnetic field generated by the whole block, we need to calculate the following integral

$$B_z = \frac{\mu_0 M_0}{\pi} \int_{-L}^{0} \frac{ab(2(d-z)^2 + a^2 + b^2)}{((d-z)^2 + a^2)((d-z)^2 + b^2)((d-z)^2 + a^2 + b^2)^{1/2}} dz \quad (1.8)$$

This integral cannot be calculated with MATLAB due to complexity. However, assuming that $b \gg a$, which is acceptable looking at a sedan from the front, we can simplify (7) as follows

$$B_{z-fs} \cong \frac{\mu_0 m_0}{\pi} \frac{ab(2d^2 + a^2)}{d^2(d^2 + a^2)^{3/2}}$$

Hence the magnetic field generated by the whole block is given by

$$B_z \cong \frac{\mu_0 M_0 ab}{\pi} \int_{-L}^{0} \frac{(2(d-z)^2 + b^2)}{(d-z)^2((d-z)^2 + b^2)^{3/2}} dz$$
$$= \frac{\mu_0 M_0 ab}{\pi} \left(\frac{1}{d(b^2 + d^2)^{1/2}} - \frac{1}{(d+L)(b^2 + (d+L)^2)^{1/2}} \right)$$

Considering the size of a sedan, it is reasonable to ignore the second term $(d + L >> d)$. Also for small values of , we can use the following approximation.

$$B_z \cong \frac{\mu_0 M_0 ab}{\pi} \frac{1}{d(b^2 + d^2)^{1/2}} = \frac{\mu_0 M_0 a}{\pi} \frac{1}{d\left(1 + (\frac{d}{b})^2\right)^{1/2}} \cong \frac{\mu_0 M_0 a}{\pi d} \quad (1.9)$$

If there is any existing magnetic field at point A, like the earth's magnetic field, a constant needs to be added to equation (9) to obtain the total magnetic field, resulting in equation (10)

$$First\ Approximation \qquad B_z \cong \frac{pb}{d(b^2 + d^2)^{\frac{1}{2}}} + q \quad (1.10)$$

$$Second\ Approximation \qquad B_z \cong \frac{p}{d} + q \tag{1.11}$$

It should be noted that the second approximation is only valid for small values of d.

The analytical equation developed here will be compared with experimental data for a number of vehicles in the next chapter and an adaptive position estimation algorithm will be developed.

2 One-Dimensional Relative Vehicle Position Estimation and Crash Detection

An AMR sensor has a silicon chip with a thick coating of piezoresistive nickel-iron. The presence of an automobile in close range causes a change in magnetic field which changes the resistance of the nickel-iron layer. The 3-axis HMC 2003 set of AMR devices from Honeywell were utilized for the system developed in this project. Application note AN218 from Honeywell describes the use of the HMC chips for vehicle detection and traffic counting applications (neither of which involves vehicle position estimation).

The first step in order to check if AMR sensors can be used for proximity measurements is to see if there is a reliable relation between magnetic field and vehicle distance.

2.1 AMR Sensors and Magnetic Field Measurements

A number of tests with different vehicles were performed in order to experimentally investigate the magnetic field generated by an encountered vehicle as a function of distance. Figure 2.1 shows a general schematic of the tests. An AMR sensor and a sonar sensor were packaged on a PCB together with a microprocessor that read the sensor signals and transmitted their values to a computer.

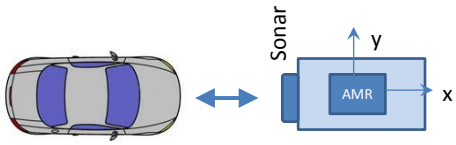

Figure 2.1: General scenario of the experiments

The outputs of the AMR and sonar sensors were sampled at the rate of 2 KHz using a dsPIC microcontroller with 12-bit ADC. Figure 2.2 shows the relationship between the magnetic field (in the X direction) and actual distance obtained from a sonar sensor for a typical test using a Chevy Impala vehicle. Magnetic field is plotted in arbitrary voltage units, the same as what was read from the ADC of the microcontroller. It can be seen that there is obviously a nonlinear relation between the measured magnetic field and distance.

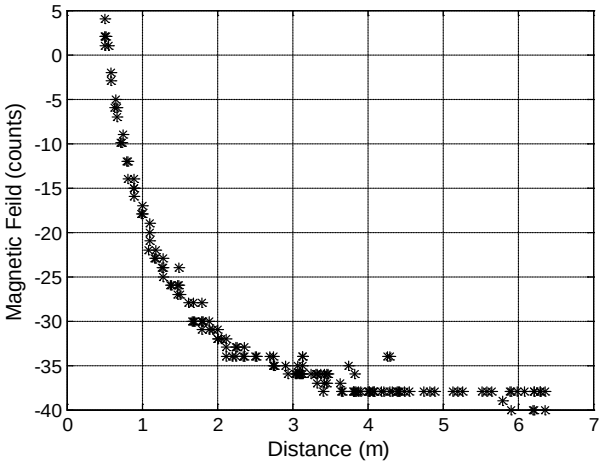

Figure 2.2: Result of the experiments with Chevy Impala showing magnetic field in X direction versus distance obtained from sonar sensor

Based on experimental data and the analytical expressions developed in the previous chapter, it was observed that below a threshold distance, x_{th}, the following relation between magnetic field and distance holds

$$B = \frac{p}{x} + q \tag{2.1}$$

where B is the magnetic field, x is distance of the vehicle from the sensors, p and q are vehicle dependent parameters. This equation was fit to experimental data from various vehicles. Figures 2.3 and 2.4 show the fitting results from two experiments with a Chevy Impala and A VW Passat. In both of the experiments, the vehicle was moved from an initial distance toward the sensors. In these figures, data set 1 is the set of data points obtained after a certain time that the vehicle gets closer than x_{th} to the sensors. This data set was used for curve fitting. Data set 2 is the set of data points from the same experiment where the vehicle was further than x_{th} from the sensors and plotted for comparison.

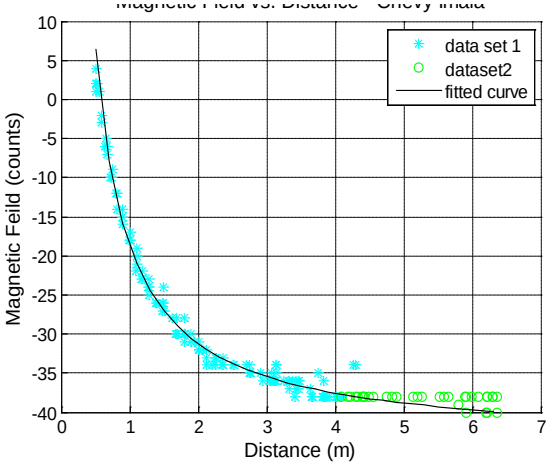

Figure 2.3: Results of the experiment with Chevy Impala and fitted curve

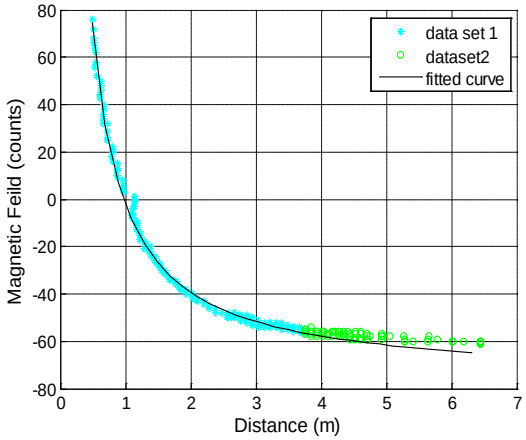

Figure 2.4: Results of the experiment with VW Passat and fitted curve

The equation was also verified against data from the same type of experiment with Hyundai Elantra and Honda Accord vehicles.

An estimate of x_{th} can be obtained even by visually inspecting the graphs or from the following fact that

$$\begin{cases} B = B_{stat} & x \geq x_{th} \\ B = \dfrac{p}{x_{th}} + q & x \leq x_{th} \end{cases} \tag{2.2}$$

where B_{stat} is the static magnetic field measured by the AMR sensor when there is no vehicle close to it. Therefore, at $x = x_{th}$, we have

$$B_{stat} = \frac{p}{x_{th}} + q \tag{2.3}$$

One can obtain an estimate of x_{th} by the following equation

$$x_{th} = \frac{p}{B_{stat} - q + e} + q \tag{2.4}$$

where e is a positive constant used to assure that the change in magnetic field is caused by the vehicle and not quantization error and noise. Table 1 summarizes the results of the experiments showing $R^2$of the fitted line and estimated x_{th} for various vehicles.

Table 2.1: Results from curve fitting

Vehicle	p	$B_{stat} - q$	R^2	x_{th}
Chevy Impala	25.26	3.23	0.997	~4.8
Honda Accord	-28.42	-6.79	0.999	~3.2
WV Passat	74.38	14.38	0.997	~4.5
Hyundai Elantra	-10.2	-3.21	0.999	~3

2.2 Technical Challenges

The next step would be to adopt the proposed equation for proximity sensing. However; it is worth mentioning here that from different experiments, it was observed that the speed of the approaching vehicle has a slight but noticeable effect on measured magnetic field. This is shown in Figure 2.5. The offsets in the magnetic fields, B_{stat}, has been subtracted from the measured data so that the difference can be illustrated better. The same trend was also seen in experiments with the Chevy Impala and the Hyundai Elantra.

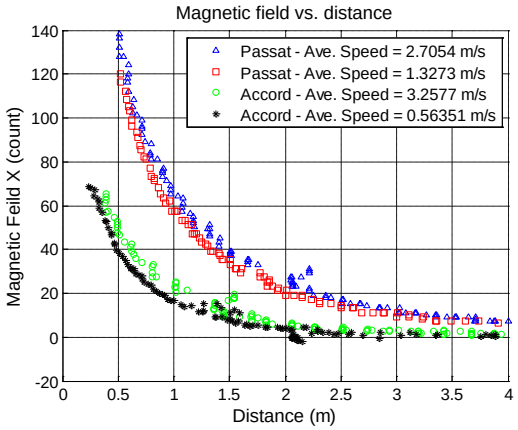

Figure 2.5: Effect of speed on measured magnetic field

The magnetic field generated by the vehicle also changes with changing the global position and orientation of the experiment. One possible explanation for this is that some of the metal in the vehicle body is magnetized in the earth magnetic field and affects the total magnetic field seen by the sensors.

Furthermore, the values of the parameters p and q vary with the vehicle, being constant for a specific vehicle but changing from one model to another. Since the type of vehicle encountered is not known apriori, these parameters have to be adaptively updated in real-time.

2.3 Iterated Extended Kalman Filter (IEKF) for Adoptive Position Estimation

In the previous section we found a relation between distance and magnetic field. Knowing parameters p and q, one would be able to estimate the distance by using only the AMR sensor. However, these parameters change from one vehicle to another vehicle and from one location to another location. Therefore, the critical challenge is to estimate p and q accurately and quickly in real time and use them to estimate the distance of the approaching vehicle from the sensors.

To address this challenge, the use of two AMR sensors located apart from each other by a distance d in the X-axis as shown in Figure 2.6, is used. The approaching vehicle is assumed to be close enough to affect both AMR sensors. The use of two sensors enables the estimation of both parameters p and q. The vehicle position can then be subsequently obtained. Figure 2.7 shows a PCB with two AMR sensors and one sonar sensor, with the dsPIC processor and other needed electronics.

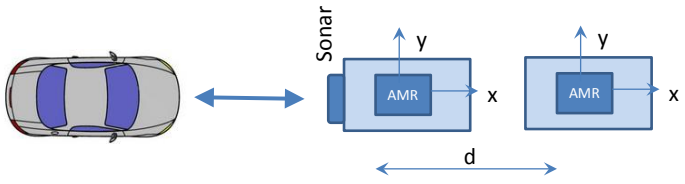

Figure 2.6: Experiments with two AMR sensors apart from each other by distance d

Figure 2.7: The developed PCB for experiments

We can write the following equations for the measured magnetic fields

$$\begin{cases} B_{1m}(t_k) = \dfrac{p}{x(t_k)} + q_1 + n_1 \\ B_{2m}(t_k) = \dfrac{p}{x(t_k) + d} + q_2 + n_2 \end{cases} \tag{2.5}$$

where B_{1m} and B_{2m} are the measured magnetic fields and n_1 and n_2 are noise. It should be noted that q_1 and q_2 are not necessarily equal since B_{1stat} and B_{2stat} can be quite different. However considering the fact that x_{th} is the same for both of the equations, we can write the following equations

$$\begin{cases} B_{1stat} = \dfrac{p}{x_{th}} + q_1 \\ B_{2stat} = \dfrac{p}{x_{th}} + q_2 \end{cases} \Longrightarrow q_2 = q_1 + \Delta B_{stat} \tag{2.6}$$

where $\Delta B_{stat} = B_{2stat} - B1_{stat}$. If we eliminate x from equations (15) and drop the time index we will have

$$\begin{aligned} dB_1(B_2 - \Delta B_{stat}) = {} & \big(B_1 - (B_2 - \Delta B_{stat})\big)p \\ & + d\big(B_1 + (B_2 - \Delta B_{stat})\big)q_1 - dq_1^2 \\ & + \big(-p - dq_1 + d(B_2 - \Delta B_{stat})\big)n_1 \\ & + (p + dB_1 - dq_1)n_2 - dn_1n_2 \end{aligned} \tag{2.7}$$

This equation can be used to estimate p and q_1 and the subsequently obtain an estimate x using equations (15). Among the various estimators, the IEKF [10], [11]seemed a reasonable choice for this nonlinear estimation problem. It should be noted that since we are not considering the dynamic equations of the vehicle, there would be no time updates for IEKF, only measurement updates. It also worth mentioning that the ordinary UKF[12], [13] estimators also fail in this

case, mainly because of the discontinuity at $x = 0$.

Putting the above relation into IEKF equations the states and noise definitions are

$$X = [p\ q_1]',\ n = [n_1\ n_2]',\ n \sim (0, R)$$

and the measurement equation is

$Z = h(X, n)$

$$Z = dB_1(B_2 - \Delta B_{stat}) \tag{2.8}$$

$$\begin{aligned} h(X,n) = {} & \big(B_1 - (B_2 - \Delta B_{stat})\big)p + d\big(B_1 + (B_2 - \Delta B_{stat})\big)q_1 - dq_1^2 \\ & + \big(-p - dq_1 + d(B_2 - \Delta B_{stat})\big)n_1 + (p + dB_1 - dq_1)n_2 - dn_1n_2 \end{aligned} \tag{2.9}$$

The measurement update equations is as follows

$$H_k = \left.\frac{\partial h_k}{\partial x}\right|_{\hat{X}_k^-} =$$

$$[B_{1,k} - \big(B_{2,k} - \Delta B_{stat}\big) \quad + d\left(B_{1,k} + \big(B_{2,k} - \Delta B_{stat}\big)\right) - 2d\hat{q}_{1,k-1}] \tag{2.10}$$

$$M_k = \left.\frac{\partial h_k}{\partial n}\right|_{\hat{X}_k^-} =$$

$$[-\hat{p}_{k-1} - d\hat{q}_{1,k-1} + d\big(B_{2,k} - \Delta B_{stat}\big)$$

$$\hat{p}_{k-1} + dB_{1,k} - d\hat{q}_{1,k-1}]$$

$$K_k = P_{k-1}H_k^T(H_kP_{k-1}H_k^T + M_kR_kM_k^T)^{-1}$$

$$\hat{X}_k = \hat{X}_{k-1} + K_k[Z_k - h_k\big(\hat{X}_{k-1}, 0\big)]$$

$$P_k = (I - K_kH_k)P_{k-1} \tag{2.11}$$

Applying the estimator to data obtained from experiments we should be able to estimate p and q_1 and by using them we should get an estimate of distance. To verify this more tests were performed in which the vehicle moved toward the sensors from a distance and sensor outputs were recorded. Then a portion of data in which according to sonar sensor, the vehicle was closer

than x_{th} to the sensors (or the AMR sensors seemed visually to be responding to the approaching vehicle) was selected and the designed IEKF estimator was applied. The results are shown in Figures 2.8 to 2.12.

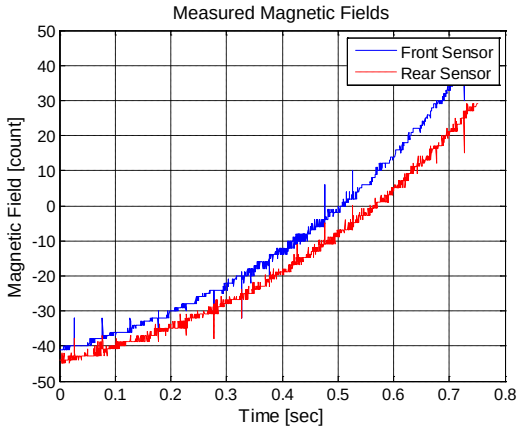

Figure 2.8: Sensed magnetic fields over time

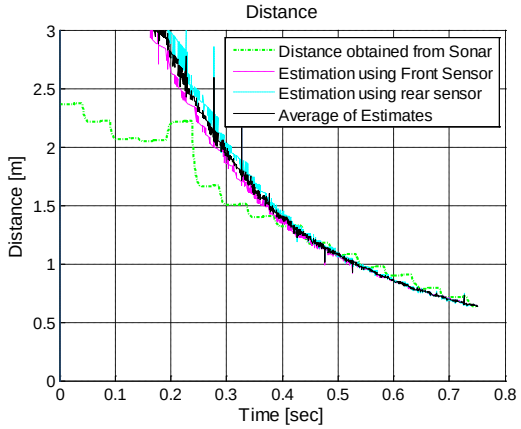

Figure 2.9: Distance obtained from sonar sensor and estimated distances

It can be seen that the parameters p and q both converge in a period of about 0.6 seconds. The resulting position estimation as seen in Figure 2.9 also converges very well to the position measured by the sonar sensor.

Being a nonlinear estimator, there are some issues with the designed estimator. First of all, the states appear not only in H_k but also in M_k. This would make the nonlinear estimator sensitive to initial conditions. Although q_1 would be close to B_{1stat} and $q_{1,0}$ can be set close to its real value, p changes a lot from one vehicle to another vehicle as shown in Table 1. It can be seen from figure 2.9 the initial value for p was chosen to be 100, not far from the final value. In this example initial values higher than ~100 will cause the estimator not to converge in the time considered. This is a very critical issue for imminent crash detection. Very low initial values will also sometime cause the estimator to diverge. One possible explanation is that very low initial values will make the covariance of noise generally lower than what is in reality. On the other

hand, one may argue that an appropriate initial condition can be selected using trial-and-error for different vehicles, however; p changes a lot from one vehicle to another vehicle. In addition to initial values of states, initial values of the covariance of states also play a role in convergence time and should be selected wisely.

To address these issues, sensor fusion techniques that combine both AMR and sonar sensors were developed which are discussed in the following section.

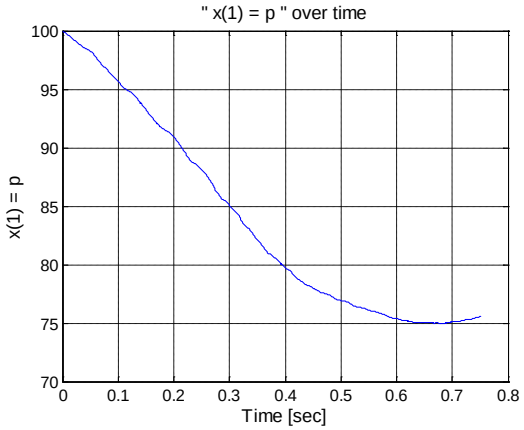

Figure 2.10: Estimated p over time

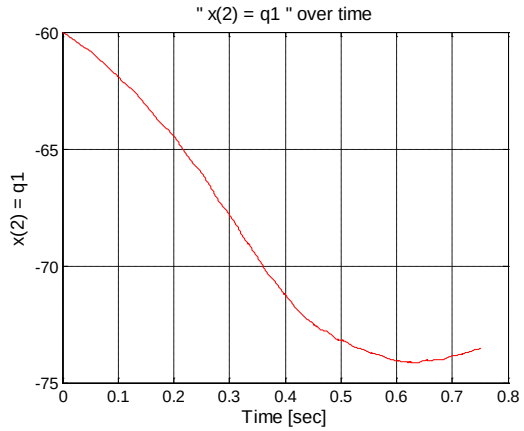

Figure 2.11: Estimated q_1 over time

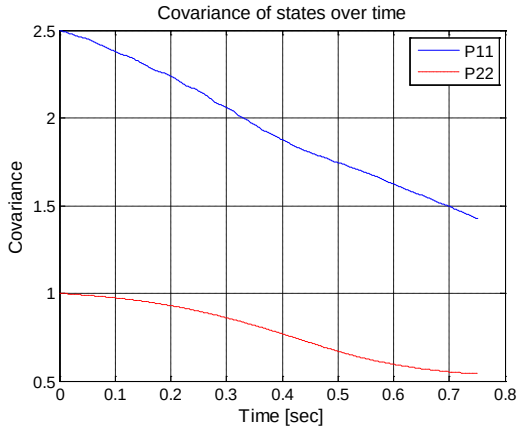

Figure 2.12: Covariance of states p and q over time

2.4 Sensor Fusion with Sonar for Improved Convergence

A sonar sensor can directly measure position independent of relative speed with respect to the sensor. It can measure larger distances compared to the AMR sensors of several feet and typically will not be able to work at very short distances below 1 or 2 feet. Furthermore, it has a narrow field of view at short distances.

A sensor fusion system can be used to exploit the advantages of both types of sensors to overcome their individual problems. Therefore a new architecture is designed for the estimator using the finite state machine shown in Figure 2.13. In state 0, the estimator will use the sonar sensor to update position, since the AMR sensors are not yet affected by the approaching vehicle. As soon as the AMR sensors respond to the approaching vehicle, updates would be done using both sonar and AMR sensors (state 1). When the vehicle enters a distance where the sonar readings are not valid any more due to very small distances, updates would be done using only the AMR sensors (state 2).

For transitions between the states in the finite state machine, x_{th} would be the best variable to utilize for switching from state 0 to 1, but there is no prior knowledge about x_{th} when a new vehicle is approaching. Therefore, the covariance of the AMR data at pre-determined time intervals can be used instead. Starting from state 0, whenever the covariance is higher than a threshold, the estimator switches to state 1 in order to switch from sonar to sonar-AMR updates. To obtain more meaningful initial values for the states p and q_1, a LS fitting can be done at the switching time. The estimated values and their covariance are used as initial values for p and q_1 and their covariance. While in state 1, x_{th} can be calculated in real-time and be used for determining if the vehicle is moving out of the view of the AMR sensors or the sonar sensor and if the system should switch back to state 0 or switch to state 2.

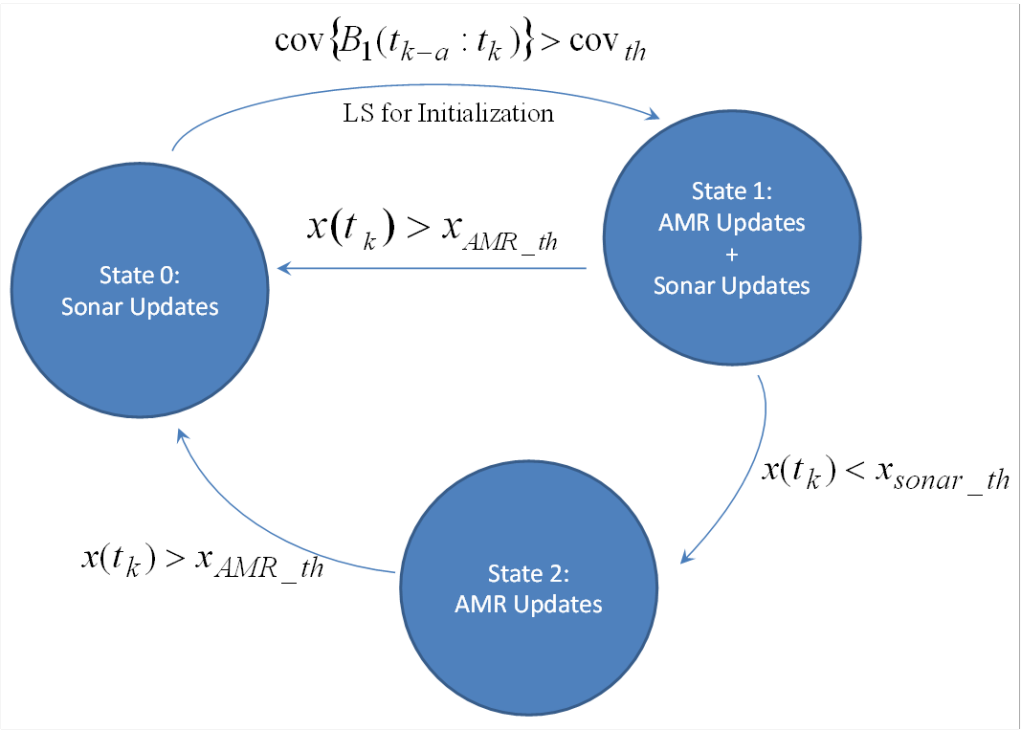

Figure 2.13: Architecture of the new estimator using sensor fusion

The next step is to develop the IEKF estimator equations for state 1 operation, where the states would be updated with both sonar and AMR sensors. The system and measurement equations are given as follows

$$X_k = FX_{k-1} + Gw_{k-1}$$

$$Z = h(X, n)$$

$$w_k \sim (0, Q_k)$$

$$n_k \sim (0, R_k)$$

where

$$X = [x \;\; v \;\; a \;\; p \;\; q_1]^T$$

$$F = \begin{bmatrix} 1 & dt & 0 & 0 & 0 \\ 0 & 1 & dt & 0 & 0 \\ 0 & 0 & 1 & 0 & 0 \\ 0 & 0 & 0 & 1 & 0 \\ 0 & 0 & 0 & 0 & 1 \end{bmatrix}, G = \begin{bmatrix} 0 & 0 \\ 0 & 0 \\ 1 & 0 \\ 0 & 1 \\ 0 & 0 \end{bmatrix}$$

$$Z = [x_s \;\; B_1 \;\; (B_2 - \Delta B_{stat})]^T$$

$$n = [n_x \;\; n_1 \;\; n_2]^T$$

$$h(X,n) = \left[x + n_x \quad \frac{p}{x} + q_1 + n_1 \quad \frac{p}{x+d} + q_1 + n_2\right]^T$$

The time update equations would be as follows

$$\hat{X}_k^- = f_{k-1}(\hat{X}_{k-1}^+, u_{k-1}, 0)$$

$$P_k^- = FP_{k-1}^+F^T + GQ_{k-1}G^T$$

The measurement update equations would be as follows

$$K_k = P_k^- H_k^T (H_k P_k^- H_k^T + M_k R_k M_k^T)^{-1}$$

$$\hat{X}_k^+ = \hat{X}_k^- + K_k[Z_k - h_k(\hat{X}_k^-, 0)]$$

$$P_k^+ = (I - K_k H_k)P_k^-$$

where

$$H_k = \frac{\partial h_k}{\partial X}\bigg|_{\hat{X}_k^-} = \begin{bmatrix} 1 & 0 & 0 & 0 & 0 \\ -\frac{p}{x^2} & 0 & 0 & \frac{1}{x} & 1 \\ -\frac{p}{(x+d)^2} & 0 & 0 & \frac{1}{x+d} & 1 \end{bmatrix}\Bigg|_{\substack{x = \hat{x}_k^- \\ p = \hat{p}_k^- \\ q_1 = \hat{q}_{1,k}^-}} \tag{2.12}$$

$$M_k = \begin{bmatrix} 1 & 0 & 0 \\ 0 & 1 & 0 \\ 0 & 0 & 1 \end{bmatrix} \tag{2.13}$$

Now based on the value of the current state, the appropriate updates can be performed. The estimator is then tested using experiments. The following experiments were performed to check the estimator. A VW Passat car approached the sensors and moved away (between 5 and 15 seconds), then a Chevy Impala came close to the sensors and moved away (between 20 and 30 seconds). The results are shown in figures 2.14 to 2.20. The red circles in these figures indicate the time at which a change transitions in the finite state machine occurred.

As can be seen from the figures, the algorithm proposed to switch between states and get an initial value for p and q_1 works very well. Excellent estimation of distance is obtained as seen in Figure 2.15. This is inspite of the change in vehicles that occurs between the VW Passat and the Chevy Impala during the experiment. As seen in Figure 18, p converges quickly and changes in value between the two vehicles. Likewise the parameter q also changes in value between the two vehicles. It can be also seen that the final values of sonar distance and estimated distance in each scenario are not exactly the same. At this point it is not clear if this is due to the inaccuracy of sonar sensor or AMR estimation and needs to be considered further.

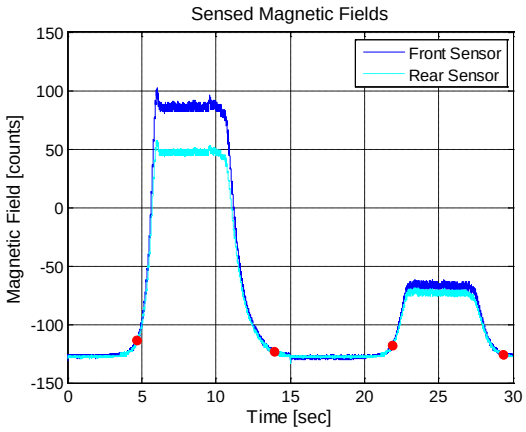

Figure 2.14: Sensed magnetic fields over time

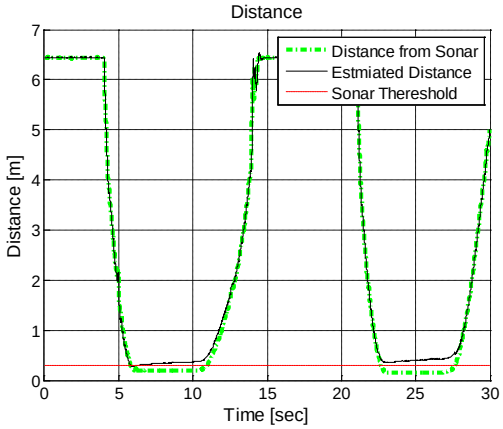

Figure 2.15: Distance obtained from sonar sensor, estimated distance and sonar threshold below which the sonar data is ignored

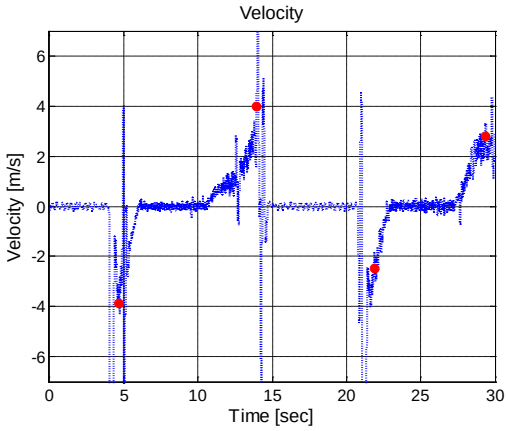

Figure 2.16: Estimated velocity

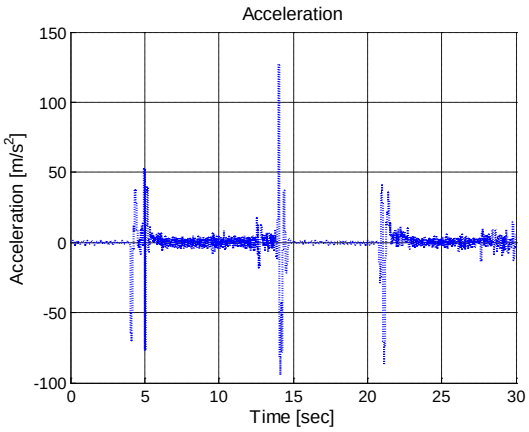

Figure 2.17: Estimated acceleration

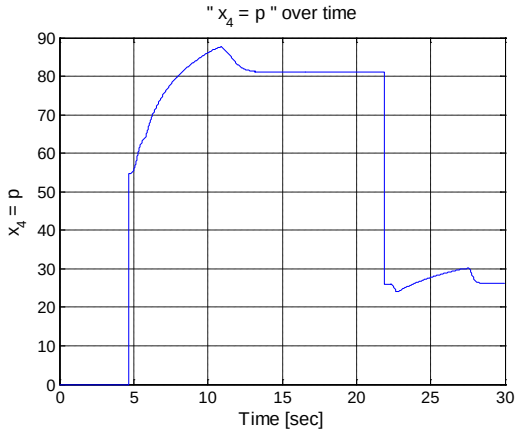

Figure 2.18: Estimated *p*

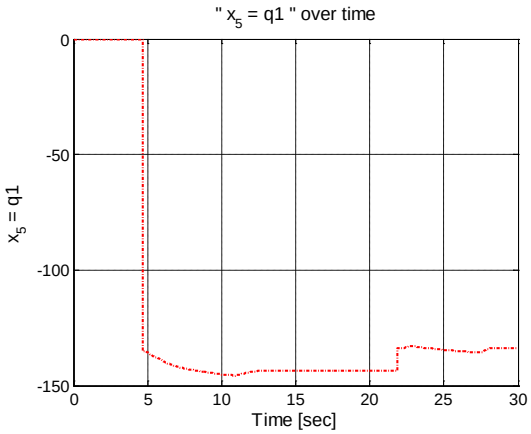

Figure 2.19: Estimated *q*

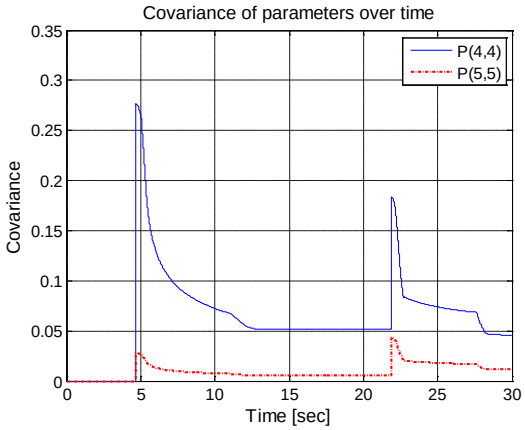

Figure 2.20: Covariance of *p* and *q*

2.5 Side Impact Measurement Experiments

The previous experiment is similar to the case where a vehicle is approaching the side of the host vehicle equipped with the imminent crash detection system.

A new experiment was required to consider the case that the host vehicle, with the imminent crash detection system, is approaching the side of another vehicle for a side impact accident. Therefore, the door of a Ford vehicle was used as a part of the side of the vehicle and was put on a cart, so that it could be moved towards and away from the sensors. This is shown in Figure 2.21.

Figure 2.21: The door of a Ford vehicle used for experiments

On the other hand, to make sure that the sensor also works at very short distances, where the sonar doesn't work, narrow marking strips were fixed to the ground apart from each other by 10 cm. Using the strips, we could compare the steady state values of distance from the designed estimator with actual marked distance. The results are shown in Figure 2.22-2.29.

It can be seen that the estimation algorithm works very well for this side impact scenario as well. The distance estimated matches the distance measured by the sonar up to 0.3 meters. It also matches the distance marked by the marking strips at smaller distances below 0.3 meters. As can

be seen from Figure 2.23, the estimator steady state value is very close to the reference line. Indeed the error is less than 1.3 cm.

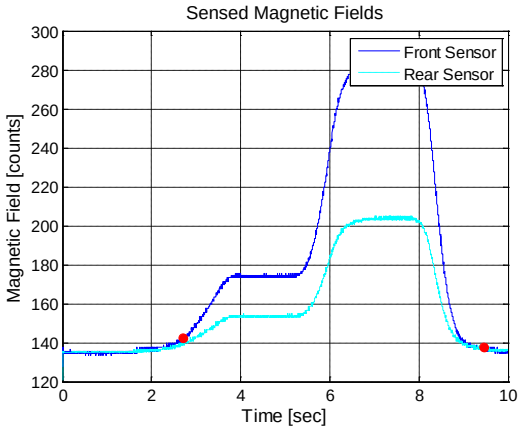

Figure 2.22: Sensed magnetic fields over time

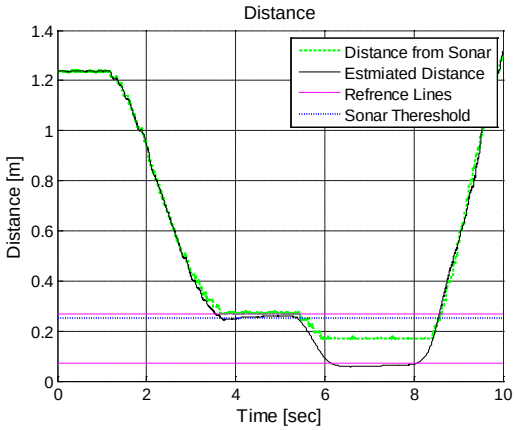

Figure 2.23: Distance obtained from sonar and estimates

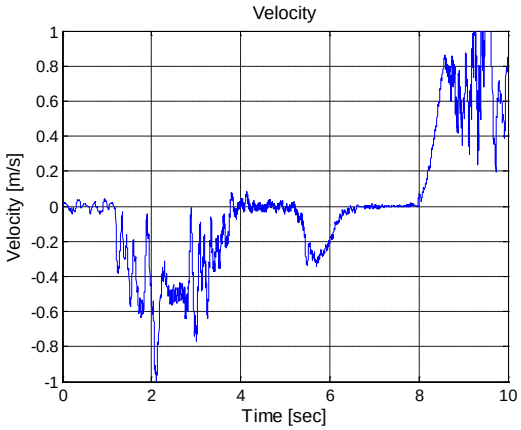

Figure 2.24: Estimated velocity

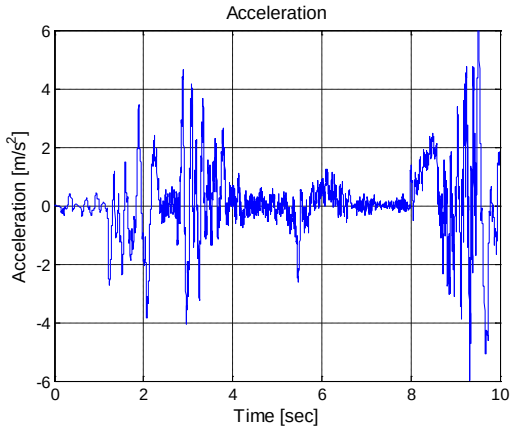

Figure 2.25: Estimated acceleration

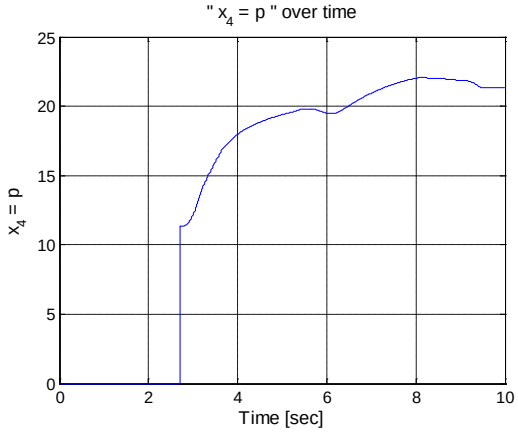

Figure 2.26: Estimated *p*

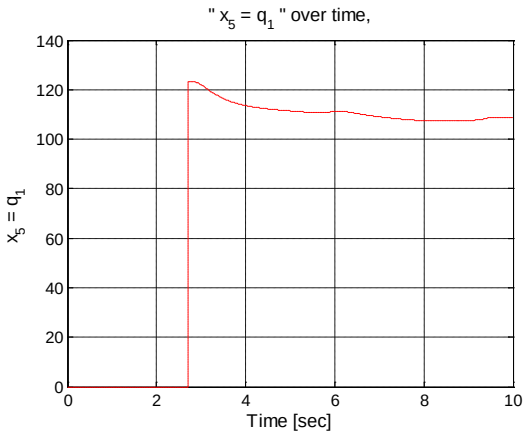

Figure 2.27: Estimated *q*

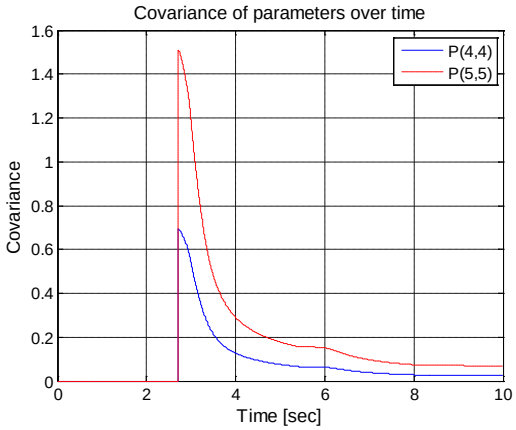

Figure 2.28: Covariance of *p* and *q*

2.6 Conclusions

This chapter focuses on the development of automotive sensors that can measure the relative position and velocity of another in close proximity, so as to enable prediction of an imminent collision just before the collision occurs. Anisotropic magnetoresistive (AMR) and sonar sensors are adopted for development of the proposed sensor system. The challenge in the use of the AMR sensors include their nonlinear behavior, limited range and magnetic signature levels that vary with each type of car. An adaptive filter based on the extended Kalman filter (EKF) is developed to automatically tune filter parameters for each encountered car and reliably estimate car position. The usage of an additional sonar sensor during the initial detection of the encountered vehicle is shown to highly speed up the parameter convergence of the filter. Experimental results are presented from tests with a large number of various vehicles to show that the proposed sensor system is viable. The developed sensors represent perhaps the first ever system that can measure relative vehicle position at close proximity right up to the point where a crash occurs. The results in this chapter have shown that it is possible to have an adaptive estimator that can adapt to the AMR sensor parameters which are dependent on the specific vehicle encountered.

3 Two-Dimensional Relative Position Estimation

3.1 Introduction

For the 1-D motion, in which the vehicle or the door is moving directly toward the sensors, we found that below a threshold distance, x_{th}, the following relation between magnetic field and distance can be assumed.

$$B = \frac{p}{x} + q \qquad x \leq x_{th} \tag{3.1}$$

Using the above relation and putting it into an IEKF estimator with the measurements from two AMR sensors and one Sonar sensor, the position, velocity and acceleration of a vehicle could be estimated. The next step is to estimate position, velocity and acceleration of a vehicle moving in 2-D, meaning that the target vehicle can have different orientations with respect to the sensors.

To further investigate the 2-D motion problem, first consider the simplified case in which the vehicle is moving toward the sensors at a constant angle, as shown in Figure 3.1. In this case, if the angle θ is known, we can obtain the magnetic field along the direction of motion of the vehicle from the AMR sensors' measurements as follows

$$B = B_{xAMR}\cos\theta - B_{yAMR}\sin\theta = \frac{p}{x} + q \tag{3.2}$$

and be able to use the designed IEKF estimator.

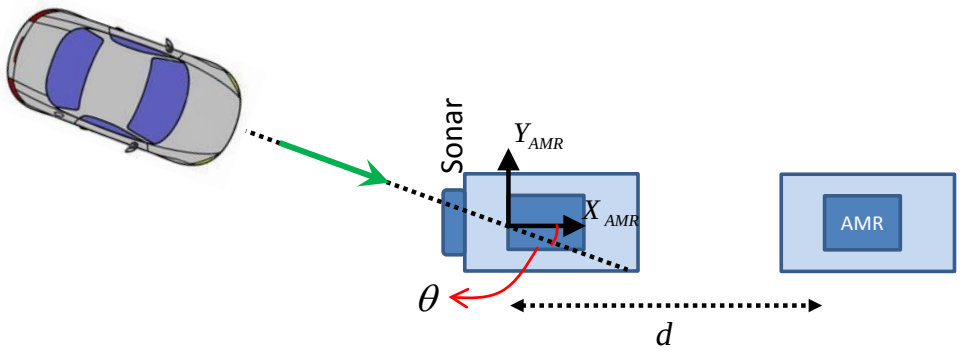

Figure 3.1: Vehicle moving toward sensors at a constant angle

However, if θ is not constant, or if the vehicle is moving toward the sensors at an offset (meaning that its centerline does not pass through the center of the AMR sensor), then th above approach cannot be used.

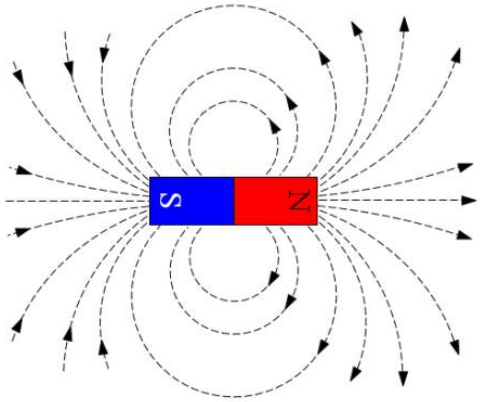

Figure 3.2: Magnetic field lines of a magnetic bar

Estimation of vehicle position in 2-D motion is much more complicated than in the 1-D motion case not only because of the additional DOF for the vehicle, but also because of the complex pattern of the vehicle's magnetic field in 2-D space. The magnetic field lines are not parallel to each other and they curve out to the sides. This is the same with any type of magnets. Figure 3.2 shows the magnetic field lines of a rectangular magnet.

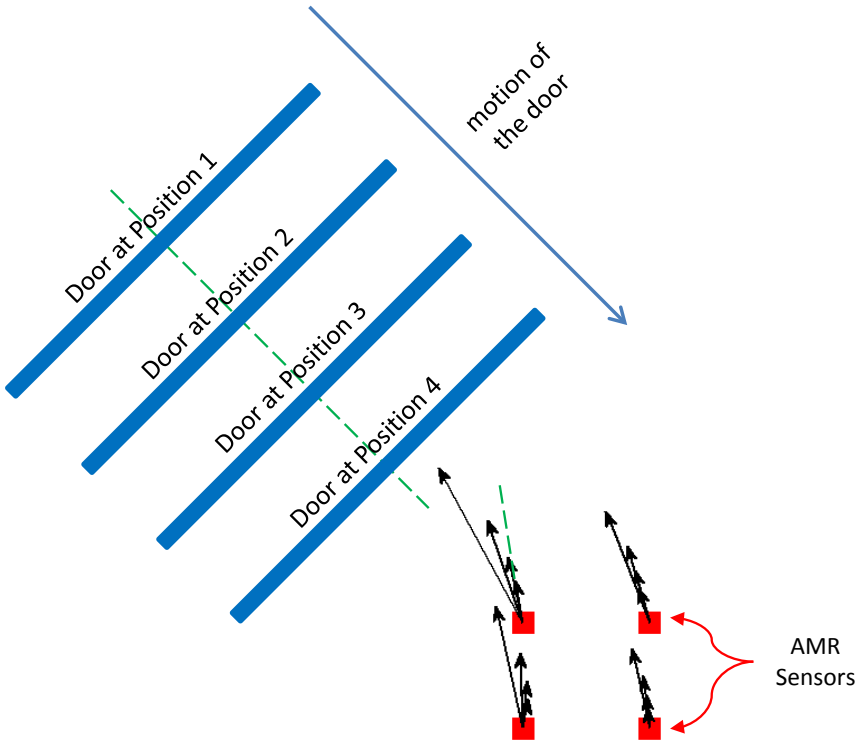

Figure 3.3: Magnetic field of the door while moving toward AMR sensors at 45 degrees

This can be also observed from the data obtained from experiments with the car door. Figure 3.3 shows a case where the door is coming toward four AMR sensors at a 45 degree angle. The sensor readings at four different locations of the door during its motion are shown. As seen in the figure, initially the direction of the field is very different from the normal direction of the door (shown with green dashed line in Figure 3.3). Hence it is not possible to obtain the orientation of the door, θ, by only determining the direction of the magnetic field. It can be also seen that as the door gets closer, the magnetic field magnitude increases and its direction changes to become in line with the normal direction of the door.

To further investigate magnetic field in 2-D, a mathematical expression for the field in a 2-D plane created by a magnet is derived in the next section.

3.2 Derivation of a Mathematical Expression for Magnetic Field in 2-D

Earlier, we obtained an expression for the magnetic field of a rectangular block of magnetic dipoles along its x axis as a function of x with the assumption that the height of the block is much smaller than the width of the block. However, to estimate the position of a vehicle in 2-D, we need to obtain the magnetic field not only along one axis and in one direction, but in 2-D space. In other words, looking at Figure 3.4, we want to obtain the magnetic field B, at an arbitrary point A. The goal is to later use the derived equations and estimate (x_A, y_A) by measuring B_x and B_y using an AMR sensor at point A. In the following derivations, the height of the block is assumed to be negligible with respect to its width and is denoted by da.

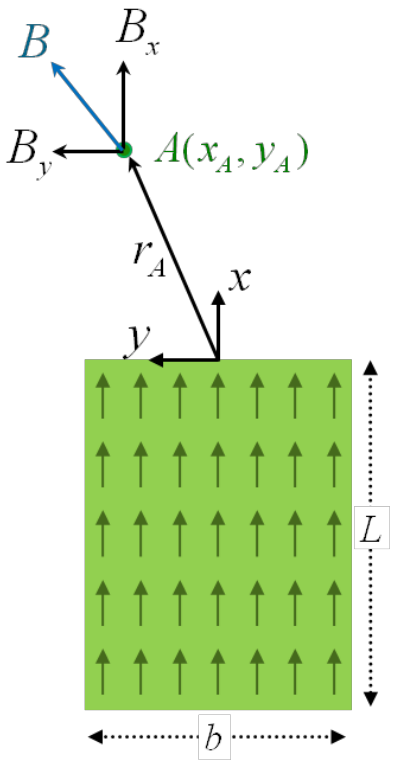

Figure 3.4: Analysis of magnetic field around a magnetic block in 2-D

As a first step, we obtain the magnetic field of a line of magnets as shown in Figure 3.5.

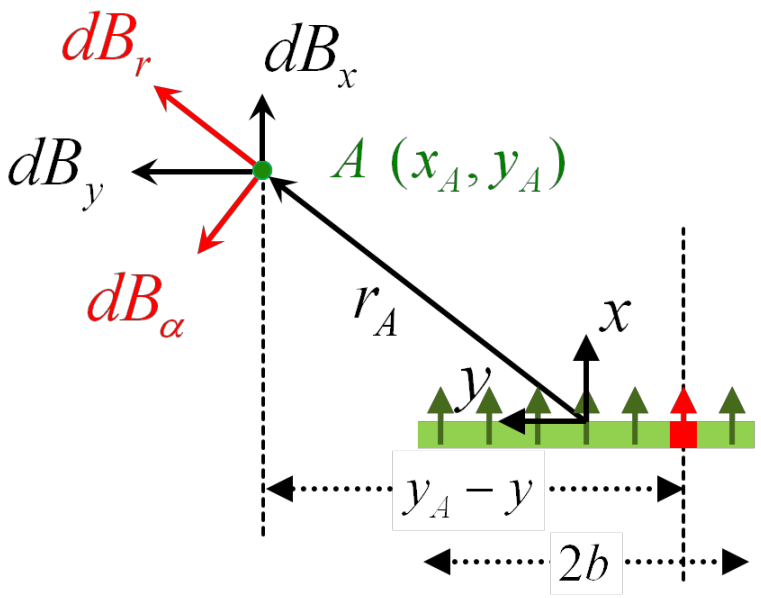

Figure 3.5: Analysis of magnetic field of line of dipoles

The following relations can be written down:

$$dB_r = \frac{\mu_0 dm_0}{2\pi r^3}\cos\alpha \tag{3.3}$$

$$dB_\alpha = \frac{\mu_0 dm_0}{4\pi r^3}\sin\alpha \tag{3.4}$$

In order to obtain B_x and $B_y$we need to integrate dB_x and dB_y which are given by the following equations

$$dB_x = dB_r\cos\alpha - dB_\alpha\sin\alpha \tag{3.5}$$

$$dB_y = dB_r\sin\alpha + dB_\alpha\cos\alpha \tag{3.6}$$

Expressing r and α in terms of x and y

$$r = (x_A^2 + (y_A - y)^2)^{\frac{1}{2}} \tag{3.7}$$

$$\alpha = \operatorname{atan}\left(\frac{y_A - y}{x_A}\right) \tag{3.8}$$

$$\sin\alpha = \frac{y_A - y}{(x_A^2 + (y_A - y)^2)^{\frac{1}{2}}} \tag{3.9}$$

$$\cos\alpha = \frac{x_A}{(x_A^2 + (y_A - y)^2)^{\frac{1}{2}}} \tag{3.10}$$

Hence

$$dB_x = \frac{\mu_0 dm_0}{4\pi r^3}(2\cos^2\alpha - \sin^2\alpha) = \frac{\mu_0 dm_0}{4\pi}\frac{2x_A^2 - (y_A - y)^2}{(x_A^2 + (y_A - y)^2)^{\frac{5}{2}}} \tag{3.11}$$

$$dB_y = \frac{\mu_0 dm_0}{4\pi r^3}3\cos\alpha\sin\alpha = \frac{\mu_0 dm_0}{4\pi}\frac{3x_A(y_A - y)}{(x_A^2 + (y_A - y)^2)^{\frac{5}{2}}} \tag{3.12}$$

We can obtain the magnetic field generated by the line of magnetic dipoles by integrating the above terms

$$B_{x-l}(x_A, y_A) = \frac{\mu_0 m_0 da\, dx}{4\pi}\int_{-b}^{b}\frac{2x_A^2 - (y_A - y)^2}{(x_A^2 + (y_A - y)^2)^{\frac{5}{2}}}dy$$
$$= \frac{\mu_0 m_0 da\, dx}{4\pi}\left(\frac{2x_A^2(\mathrm{y_A} + \mathrm{b}) + (y_A + b)^3}{x_A^2(x_A^2 + (y_A + b)^2)^{\frac{3}{2}}} - \frac{2x_A^2(\mathrm{y_A} - \mathrm{b}) + (y_A - b)^3}{x_A^2(x_A^2 + (y_A - b)^2)^{\frac{3}{2}}}\right)$$

$$B_{y-l}(x_A, y_A) = \frac{\mu_0 m_0 da\, dx}{4\pi}\int_{-b}^{b}\frac{3x_A(y_A - y)}{(x_A^2 + (y_A - y)^2)^{\frac{5}{2}}}dy$$
$$= \frac{m_0 da\, dx}{4\pi}\left(-\frac{x_A}{x_A^2(x_A^2 + (y_A + b)^2)^{\frac{3}{2}}} + \frac{x_A}{x_A^2(x_A^2 + (y_A - b)^2)^{\frac{3}{2}}}\right)$$

In order to obtain the total magnetic field created by the whole bar, we can integrate B_{x-l} and B_{y-l} in the X direction as follows.

$$B_x = \int_{x_A}^{x_A+L} B_{x-l}(x, y_A)$$

$$= \frac{\mu_0 m_0 da}{4\pi}\left(- \frac{y_A + b}{(x_A + L)((x_A + L)^2 + (y_A + b)^2)^{\frac{1}{2}}} \right.$$

$$+ \frac{y_A - b}{(x_A + L)((x_A + L)^2 + (y_A - b)^2)^{\frac{1}{2}}} + \frac{y_A + b}{x_A(x_A^2 + (y_A + b)^2)^{\frac{1}{2}}}$$

$$\left. - \frac{y_A - b}{x_A(x_A^2 + (y_A - b)^2)^{\frac{1}{2}}} \right)$$

$$B_y = \int_{x_A}^{x_A+L} B_{y-l}(x, y_A)$$

$$= \frac{\mu_0 m_0 da}{4\pi}\left(\frac{1}{((x_A + L)^2 + (y_A + b)^2)^{\frac{1}{2}}} - \frac{1}{((x_A + L)^2 + (y_A - b)^2)^{\frac{1}{2}}} \right.$$

$$\left. - \frac{1}{(x_A^2 + (y_A + b)^2)^{\frac{1}{2}}} + \frac{1}{(x_A^2 + (y_A - b)^2)^{\frac{1}{2}}} \right)$$

Assuming $x_A + L \gg x_A$ the above equations can be simplified to

$$B_x = \frac{\mu_0 m_0 da}{4\pi}\left(\frac{y_A + b}{x_A(x_A^2 + (y_A + b)^2)^{\frac{1}{2}}} - \frac{y_A - b}{x_A(x_A^2 + (y_A - b)^2)^{\frac{1}{2}}} \right) \quad (3.13)$$

$$B_y = \frac{\mu_0 m_0 da}{4\pi}\left(- \frac{1}{(x_A^2 + (y_A + b)^2)^{\frac{1}{2}}} + \frac{1}{(x_A^2 + (y_A - b)^2)^{\frac{1}{2}}} \right) \quad (3.14)$$

If now we assume that y_A is small and close to zero, we can further simply the above equations to the following

$$B_x = \frac{\mu_0 m_0 da}{2\pi} \frac{b}{x_A (x_A^2 + b^2)^{\frac{1}{2}}} + f(p, b, x_A) y^2 + \cdots = \frac{\mu_0 m_0 da}{2\pi} \frac{b}{x_A (x_A^2 + b^2)^{\frac{1}{2}}} \tag{3.15}$$

$$B_y = \frac{\mu_0 m_0 da}{2\pi} \frac{b}{(x_A^2 + b^2)^{\frac{3}{2}}} y + f(p, b, x_A) y^3 + \cdots = \frac{\mu_0 m_0 da}{2\pi} \frac{by}{(x_A^2 + b^2)^{\frac{3}{2}}} \tag{3.16}$$

It should be noted that the first equation is the same as the equation obtained earlier for 1-D case replacing da with $2a$.

Using the same assumption as in 1-D case, for small vales of x_A the above equations for can be simplified further as follows.

$$B_x = \frac{\mu_0 m_0 da}{2\pi x_A} = \frac{p}{x_A} \tag{3.17}$$

$$B_y = \frac{\mu_0 m_0 da}{2\pi} \frac{by}{(x_A^2 + b^2)^{\frac{3}{2}}} = \frac{pby}{(x_A^2 + b^2)^{\frac{3}{2}}} \tag{3.18}$$

If there is any existing static magnetic field at point A, like the earth's magnetic field, a constant needs to be added to the above equation to obtain the total magnetic field.

$$B_x = \frac{p}{x_A} + q_x \tag{3.19}$$

$$B_y = \frac{pby}{(x_A^2 + b^2)^{\frac{3}{2}}} + q_y \tag{3.20}$$

It is also possible to subtract the static magnetic field at the location of AMR sensors from measurements to avoid adding a constant for readings from each AMR sensors. However, for reading of B_x it was observed that even when subtracting the static magnetic field from the measurements, using equation (3.19) results into better fits compared to using equation (3.17). Therefore, the following equations are being used for position estimation in the next sections of

this chapter.

$$B_x = \frac{p}{x_A} + q \tag{3.21}$$

$$B_y = \frac{pby}{(x_A^2 + b^2)^{\frac{3}{2}}} \tag{3.22}$$

In the next section, the estimator for determination of vehicle position using these magnetic equations is described.

3.3 Estimator Design

In this section the estimator designed for real time 2-D position estimation of the vehicle is described. The system consists of one sonar transmitter, two sonar receivers and 4 AMR sensors. 3.6 shows the arrangement of the sensors.

In order to express the position of the object, x_A, y_A and θ should be estimated. x_A and y_A show the position of point A with respect to the coordinate frame attached to the object and θ is the angle between the X axis of the coordinate frame attached to the object and X axis of the coordinate frame at point A.

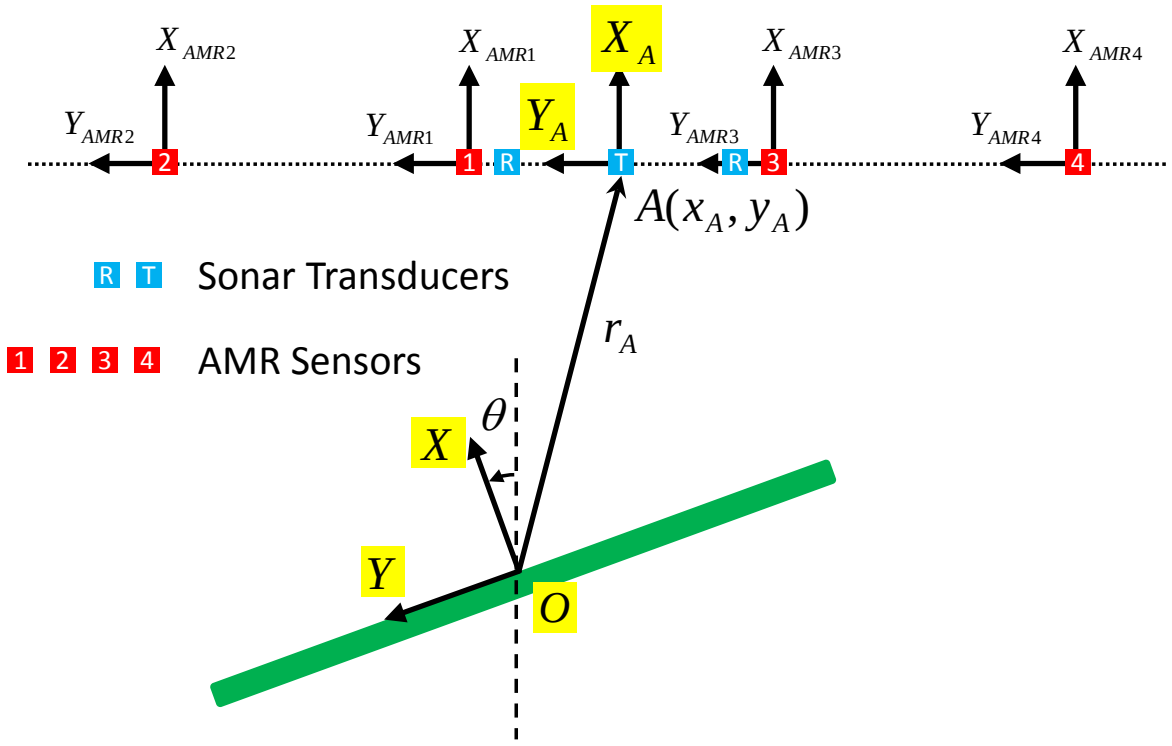

Figure 3.6: Sensors' arrangements for 2-D position estimation

The object is assumed to have a longitudinal velocity v in its X axis direction and a rotational velocity ω. The dynamics equations of the system are derived in the following section.

Another way of expressing the position of the object is to express the position of point O with respect to coordinate frame attached to point A. However, using this coordinate frame the measurement equations will be more complicated.

The combination of one sonar transmitter and two sonar receivers makes it possible to measure the distance, x_A and orientation, θ, of the approaching object. This is described in the coming sections.

On the other hand with the AMR sensors placed at a distance from each other, at each measurement update the two sensors that have smaller values of B_y ($B_{yi} = B_{yAMRi}\cos\theta - B_{xAMRi}\sin\theta$) are selected. Then B_{xAMRi} and B_{yAMRi} measurements of those two sensors are included in the measurement update using equation (b). This procedure is also described in later sections.

3.3.1 Dynamic Equations

As it was mentioned earlier, it is assumed that the object moves with a longitudinal velocity v in its X axis direction and a rotational velocity ω. Using the transport theorem we can write the

dynamic equations as follows

$$\dot{r}_A = (\dot{r_A})_{rel} + \omega \times r_A \quad \Rightarrow \quad \dot{x}_A = -v + \omega y_A \quad \& \quad \dot{y}_A = -\omega x_A \tag{3.23}$$

Discretizing the above equations, dropping A index and including longitudinal and rotational accelerations we will have the following equations for the dynamics of the systems

$$\begin{aligned} x_k &= x_{k-1} - v_{k-1}dt + \omega_{k-1}y_{k-1}dt \\ y_k &= y_{k-1} - \omega_{k-1}x_{k-1}dt \\ v_k &= v_{k-1} + a_{k-1}dt \\ \theta_k &= \theta_{k-1} + \omega_{k-1}dt \\ \omega_k &= \omega_{k-1} + \alpha_{k-1}dt \end{aligned} \tag{3.24}$$

The above equations are later used in the development of the estimator.

3.3.2 Sonar Measurement System

The second version of the Sonar sensors includes one transmitter, T, at point A and two receivers, R_1 and R_2, at distance d_1 and d_2 from A arranged in the order shown in Figure 3.6 and Figure 3.7. This configuration of the transmitter and receivers makes it possible to measure the orientation of the target in addition to the distance from the target. Measuring the travel time of sound for receivers 1 and 2, the distance that echo pulse has traveled can be calculated. Due to the fact that the incident and reflected angle of sound are equal (similar to light when reflects from mirror), it can be concluded that the measured distances equal l_1 and l_2 shown in **Error! Reference source not found.**3.7. In other words, l_1 and l_2 equal the distance from the image of transmitter T at point B to the receivers R_1 and R_2 respectively.

Knowing l_1 and l_2 and the distance between the transmitter and the receivers, d_1 and d_2 , we can calculate θ_2 using the cosine rule as follows

$$d_s = d_1 + d_2 \tag{3.25}$$

$$l_1^2 = d_s^2 + l_2^2 - 2d_s l_2 \cos(90 - \theta_2) \tag{3.26}$$

$$\theta_2 = \text{asin}\left(\frac{d_s^2 + l_2^2 - l_1^2}{2d_s l_2}\right) \tag{3.27}$$

Knowing θ_2, we can calculate l_s, the distance between the transmitter and its image ($\overline{AB}$), using the cosine rule as follows

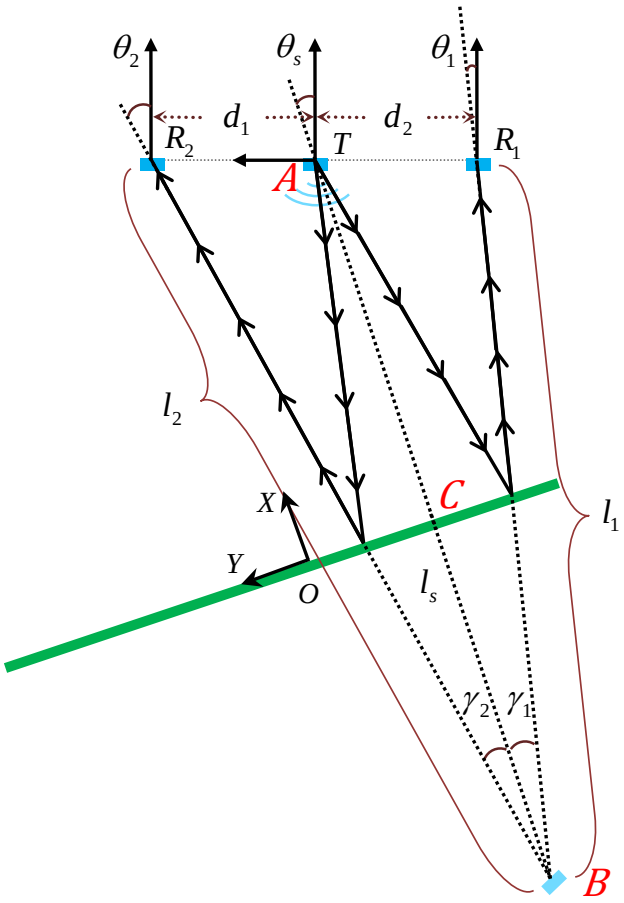

Figure 3.7: Sonar system with one transmitter and two receivers

$$l_s^2 = d_2^2 + l_2^2 - 2d_2 l_2 \cos(90 - \theta_2) \tag{3.28}$$

Then x_A ($\overline{AC}$) can be calculated from l_s since

$$x_A = \frac{l_s}{2}$$

Applying cosine rule one more time, θ_s can be also calculated

$$l_2^2 = d_2^2 + l_s^2 - 2d_2 l_s \cos(90 + \theta_s) \tag{3.29}$$

$$\theta_s = \text{asin}(\frac{l_2^2 - d_2^2 - l_s^2}{2 d_2 l_s}) \tag{3.30}$$

In practice, the measured signals from the sonar sensors are l_{1m} and l_{2m} where

$$l_{1m} = l_1 + n_1 \qquad n_1 \sim N(0, \sigma_1)$$

$$l_{2m} = l_2 + n_2 \qquad n_2 \sim N(0, \sigma_2)$$

If we want to use x_A and θ_s in the estimator we should also calculate the covariance of noise in the measurements. Since x_D and θ_s have nonlinear relations with n_1 and n_2, we need to calculate the derivatives of x_A and θ_s with respect to n_1 and n_2 which would be as follows

$$\frac{\partial x_A}{\partial n_1} = -\frac{l_{1m}}{2 l_s}\frac{d_2}{d_s} \tag{3.31}$$

$$\frac{\partial x_A}{\partial n_2} = \frac{l_{2m}}{2 l_s}\frac{d_1}{d_s} \tag{3.32}$$

$$\frac{\partial \theta_s}{\partial n_1} = \frac{\cos(\gamma_2)}{\cos(\theta_s)}\frac{l_{1m} l_{2m}}{d_s l_s^2} \tag{3.33}$$

$$\frac{\partial \theta_s}{\partial n_2} = \frac{\cos(\gamma_1)}{\cos(\theta_s)}\frac{l_{1m} l_{2m}}{d_s l_s^2} \tag{3.34}$$

Considering the above relations two observations can be made. First, at a fixed value of θ_s, noise level of the measured θ_s decreases as the door gets closer to the sensors since γ_1 and γ_2 increase and $\cos(\gamma_1)$ and $\cos(\gamma_2)$ decrease. Second, at a fixed position of door we can see that if we equally space the receivers from transmitter ($d_1 = d_2 = d_s/2$), the distance between the sensors, $d_s/2$, does not have effect on the level of noise of x_D, however increasing d_s reduces the level of noise of θ_s. On the other hand, increasing d_s will also increase θ_1 and θ_2 which are the angles that the echo pulse enters the receivers known as beam angle. The sensitivity of the receivers reduces with increasing the beam angle and the object may not be detected any more. This trade-off should be considered while picking a value for d_s.

Similar to the Sonar sensor used for 1-D positioning, the new Sonar sensor will not also work in close proximities. Also the Sonar system will not work if the orientation of the object, θ, increases so that θ_1 and θ_2 are out of the beam angle of the receivers. It should be mentioned that the threshold θ is not constant and changes slightly with the distance from the object. Hence there cannot be a constant value for $\theta_{threshold}$. However, an easier way of detecting misreading

is at the beginning of the calculation by looking at the values obtained for θ_1 and θ_2. If they have imaginary values then a misreading is detected.

It also worth mentioning here that the Sonar system alone is not able to determine y_A. In other words, the object can move along its Y axis and the sonar readings will remain the same.

3.3.3 EKF Estimator Design

The estimator Architecture is very similar to 1-D problem IEKF estimator. As it was mentioned earlier, four AMR sensors, and three Sonar transducers are adopted for 2-D positioning. A state machine similar to the one used for 1-D positioning is used for 2-D positioning as well which is shown in Figure 3.8.

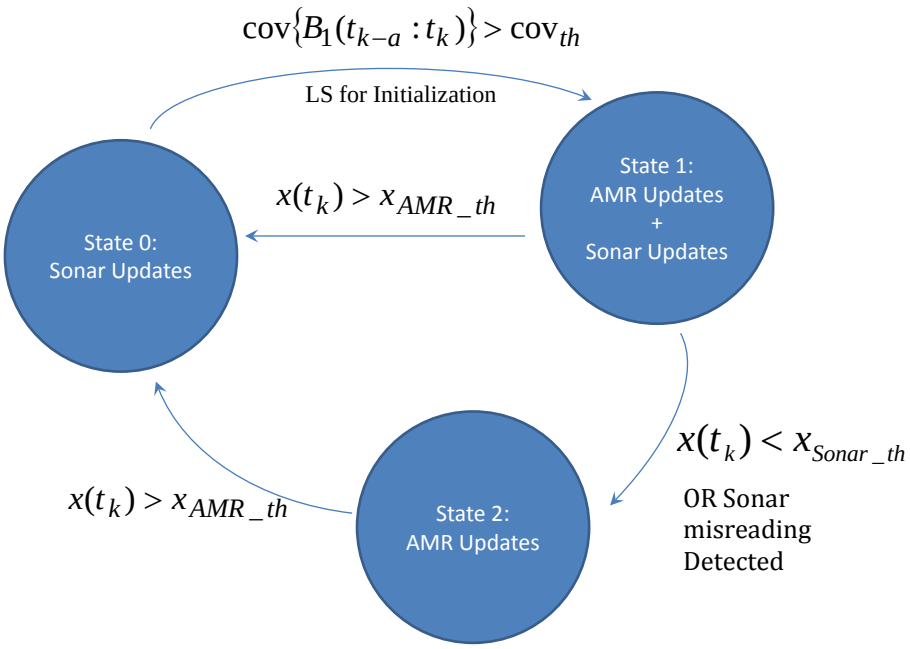

Figure 3.8: 2-D positioning state diagram

One of the differences from 1-D positioning state diagram is the transition from state 1 to state 2. The new Sonar system also measures the orientation of the object, θ, and if θ increases beyond a threshold, it will not be able to measure the orientation due to the limitations in the beam width of the Sonar transducers.

There are also some tight time constraints with real-time 2-D positioning system. Sensors data are captured through two dsPIC microcontrollers and transferred to MATLAB running on a PC at 500 Hz via serial port. Since the system is working in real-time there would be a 2-ms period of time for transferring data from microcontrollers to MATLAB (taking about .5 ms), analyzing data and visualization. Having an EKF running in MATLAB (described in later sections) it means that there is about 1.5 ms to perform time update and measurement update steps of the EKF. Therefore the measurement equations should be simplified as much as possible. For

instance it was possible to use equations obtained earlier for the magnetic field in 2-D without any simplifying assumptions however calculating the Jacobean and inverse matrix required for EKF measurement update will become complicated and time consuming. This time constraint is also the main reason for using EKF rather than IEKF.

With the above explanations, we will now derive the equations for EKF estimator. It should be noted that the equations derived here are the equations used in state 1 where both Sonar and AMR sensors are available. The state vector to be estimated is as follows

$$X = [x\ y\ v\ a\ \theta\ \omega\ \alpha\ p\ q] \tag{3.35}$$

where x, y and θ express the position of the object, v and ω are the longitudinal rotational velocity of the object, a and α are longitudinal and rotational accelerations and p and q are the equation constant for magnetic field.

The dynamic equations of the system were derived in the previous sections and result in the following equations for time update step of EKF.

$$X_k = f(X_{k-1}, w_{k-1})$$

$$x_k = x_{k-1} - v_{k-1}dt + \omega_{k-1}y_{k-1}dt$$

$$y_k = y_{k-1} - \omega_{k-1}x_{k-1}dt$$

$$v_k = v_{k-1} + a_{k-1}dt$$

$$a_k = a_{k-1} + w_{k-1}^1$$

$$\theta_k = \theta_{k-1} + \omega_{k-1}dt$$

$$\omega_k = \omega_{k-1} + \alpha_{k-1}dt$$

$$\alpha_k = \alpha_{k-1} + w_{k-1}^2$$

$$p_k = p_{k-1} + w_{k-1}^3$$

$$q_k = q_{k-1} + w_{k-1}^4$$

$$w_k \sim (0, Q_k) \tag{3.36}$$

The time update equations will be as follows

$$\hat{X}_k^- = f_{k-1}(\hat{X}_{k-1}^+, 0)$$

$$P_k^- = F_{k-1}P_{k-1}^+F_{k-1}^T + G_{k-1}Q_{k-1}G_{k-1}^T$$

$$F_{k-1} = \left.\frac{\partial f_{k-1}}{\partial X}\right|_{\hat{X}_{k-1}^{+}} = \begin{bmatrix} 1 & \hat{\omega}_{k-1}^{+}dt & -dt & 0 & 0 & \hat{y}_{k-1}^{+}dt & 0 & 0 & 0 \\ -\hat{\omega}_{k-1}^{+}dt & 1 & 0 & 0 & 0 & -\hat{x}_{k-1}^{+}dt & 0 & 0 & 0 \\ 0 & 0 & 1 & dt & 0 & 0 & 0 & 0 & 0 \\ 0 & 0 & 0 & 1 & 0 & 0 & 0 & 0 & 0 \\ 0 & 0 & 0 & 0 & 1 & dt & 0 & 0 & 0 \\ 0 & 0 & 0 & 0 & 0 & 1 & dt & 0 & 0 \\ 0 & 0 & 0 & 0 & 0 & 0 & 1 & 0 & 0 \\ 0 & 0 & 0 & 0 & 0 & 0 & 0 & 1 & 0 \\ 0 & 0 & 0 & 0 & 0 & 0 & 0 & 0 & 1 \end{bmatrix}$$

$$G_{k-1} = \begin{bmatrix} 0 & 0 & 0 & 0 \\ 0 & 0 & 0 & 0 \\ 0 & 0 & 0 & 0 \\ 1 & 0 & 0 & 0 \\ 0 & 0 & 0 & 0 \\ 0 & 0 & 0 & 0 \\ 0 & 1 & 0 & 0 \\ 0 & 0 & 1 & 0 \\ 0 & 0 & 0 & 1 \end{bmatrix} \tag{3.37}$$

As it was mentioned earlier, the sonar system with one transmitter and two receivers can provide measurements of the orientation of the object, θ, as well the distance to the object, x. There are also eight measurements from four AMR sensors B_{xAMRi}, B_{yAMRi} $(i = 1,2,3,4)$ which are measured with respect to XY coordinate frame of each AMR sensor. At each measurement update, first the measured magnetic fields at each sensor with respect to the XY coordinate frame attached to object, B_{xi} and B_{yi}, are calculated as follows

$$B_{xi} = B_{xAMRi}\cos\hat{\theta}_k^- + B_{yAMRi}\sin\hat{\theta}_k^- \tag{3.38}$$

$$B_{yi} = -B_{xAMRi}\sin\hat{\theta}_k^- + B_{yAMRi}\cos\hat{\theta}_k^- \qquad i = 1,2,3,4 \tag{3.39}$$

Second, the ratio between the magnetic fields in Y and X direction, $B_{RATi} = \frac{B_{yi}}{B_{xi}}$, is calculated for each sensor. Then the two sensors that have lower values of B_{RAT} are selected (named m and n) and the corresponding values of B_{xi} and B_{yi} of those two sensors are assigned to the new variables B_{xm}, B_{xn}, B_{ym} and B_{yn} and are used in measurement updates. This will result into the following measurement updates equations.

$$Z = h(X, n)$$

$$Z = [x_s \quad \theta_s \quad 0 \quad 0 \quad y_{meas}]^T$$

$$h(X,n) = \left[x + n_x \quad \theta + n_\theta \quad B_{xm} - \frac{p}{x + d_m \sin\theta} + q_1 + (n_{xAMRm}\cos\theta + n_{yAMRm}\sin\theta) \quad B_{xn} - \frac{p}{x + d_n \sin\theta} + q_1 + (n_{xAMRn}\cos\theta + n_{yAMRn}\sin\theta)\right]^T$$

$$K_k = P_k^- H_k^T (H_k P_k^- H_k^T + R_k)^{-1}$$

$$\hat{X}_k^+ = \hat{X}_k^- + K_k[Z_k - h_k(\hat{X}_k^-, 0)]$$

$$P_k^+ = (I - K_k H_k) P_k^-$$

(3.40)

$$H_k = \left.\frac{\partial h}{\partial X}\right|_{\hat{X}_k^-} = \left[\begin{matrix} 1 & 0 & 0 & 0 & 0 & 0 & 0 & 0 & 0 \\ 0 & 0 & 0 & 0 & 1 & 0 & 0 & 0 & 0 \\ -\frac{p}{(x + d_m \sin\theta)^2} & 0 & 0 & 0 & B_{ym} + \frac{p d_m \cos\theta}{(x + d_m \sin\theta)^2} & 0 & 0 & -\frac{1}{x + d_m \sin\theta} & -1 \\ -\frac{p}{(x + d_n \sin\theta)^2} & 0 & 0 & 0 & B_{yn} + \frac{p d_n \cos\theta}{(x + d_n \sin\theta)^2} & 0 & 0 & -\frac{1}{x + d_n \sin\theta} & -1 \\ 0 & 1 & 0 & 0 & 0 & 0 & 0 & 0 & 1 \end{matrix}\right]_{\hat{X}_k^-}$$

$$R_k = \begin{bmatrix} \sigma_{xs} & 0 & 0 & 0 & 0 \\ 0 & \sigma_{\theta s} & 0 & 0 & 0 \\ 0 & 0 & \sigma_B & 0 & 0 \\ 0 & 0 & 0 & \sigma_B & 0 \\ 0 & 0 & 0 & 0 & \sigma_{y-meas} \end{bmatrix}$$

(3.41)

where d_m and d_n are the distances from AMR sensors m and n from point A, and values in R_k matrix represent the covariance of noise in measurements and are determined through experiments and y_{meas} is a estimate of y and is obtained from equations of magnetic field in 2-D as follows

$$B_x = \frac{\mu_0 m_0 da}{2\pi} \frac{b}{x_A (x_A^2 + b^2)^{\frac{1}{2}}} \quad \& \quad B_y = \frac{\mu_0 m_0 da}{2\pi} \frac{by}{(x_A^2 + b^2)^{\frac{3}{2}}} \quad \Rightarrow$$

$$B_{RAT} = \frac{B_x}{B_y} = \frac{y x_A}{x_A^2 + b^2} \tag{3.42}$$

For each one of the selected sensors, a and b, we have the following relations

$$B_{RATm} = \frac{y_m (x + d_m \sin\theta)}{(x + d_m \sin\theta)^2 + b^2} \tag{3.43}$$

$$B_{RATa} = \frac{y_n (x + d_n \sin\theta)}{(x + d_n \sin\theta)^2 + b^2} \tag{3.44}$$

where $y_i = y + d_i \cos\theta \quad \& \quad i = m, n.$

Now using we $\hat{x}_k^-$ and $\hat{\theta}_k^-$ after each time update and the above equations we can get an estimate of y_m and y_n from the following linear equations.

$$\begin{cases} B_{RATm} T_m - y_m \left(\hat{x}_k^- + d_m \sin\hat{\theta}_k^-\right) = 0 \\ B_{RATn} T_n - y_n \left(\hat{x}_k^- + d_n \sin\hat{\theta}_k^-\right) = 0 \\ y_m - y_n = (d_m - d_n)\cos\hat{\theta}_k^- \\ T_m - T_n = \left(\hat{x}_k^- + d_m \sin\hat{\theta}_k^-\right)^2 - \left(\hat{x}_k^- + d_n \sin\hat{\theta}_k^-\right)^2 \end{cases} \tag{3.45}$$

where

$$T_i = \left(\hat{x}_k^- + d_i \sin\hat{\theta}_k^-\right)^2 + b^2 \quad \& \quad i = m, n \tag{3.46}$$

Solving for y_m, y_n, T_m and T_n we can obtain an estimation of y from the following equation

$$y_{meas} = y_m - d_m \cos\hat{\theta}_k^- \tag{3.47}$$

It should be noted that while calculating the Jacobean for EKF measurement update, the effect of x and θ on y_{meas} are ignored to make the Jacobean simpler.

3.4 Experimental Results

The developed estimator was tested with a Mazda Protégé 1999 and a Ford door. Testing with the door has the advantage that more complicated scenarios can be implemented since it is easier to move the door around.

3.4.1 Results from the Tests with a Ford Door

The estimator was also verified with tests using a Ford vehicle door. The advantage of using the door is that more complicated scenarios can be implemented since it is easier to move the door around. Here the results from one of the tests are presented. The scenario can be described as follows

- move toward the sensors at $\theta \cong 0$
- stop at $x \cong 0.6$
- rotate to $\theta \cong -30$
- move toward the sensors with constant θ
- move away from the sensors with constant θ
- rotate back to $\theta \cong 0$
- move toward the sensors at constant θ

The following Figures show the results. Figure 3.9 shows the estimated position of the door at different time intervals. The color of the line used to represent door position goes from black at the beginning to gray toward the end of the experiment. The red rectangles show the position of AMR sensors.

Figures 3.10 to 3.17 show the estimated states over time. It can be seen from Figures 3.10 and 3.14 that when the door rotates to more than the threshold angle, the sonar measurement for distance and orientation are not valid anymore and the estimator switches from state 1 to state 2 and only updates with AMR sensors. When the door rotates back toward $\theta \cong 0$ the sonar measurements become valid again and the estimator switches to state 1. Also when later in the experiment, the door gets very close to the sensors, the estimator switches to state 2.

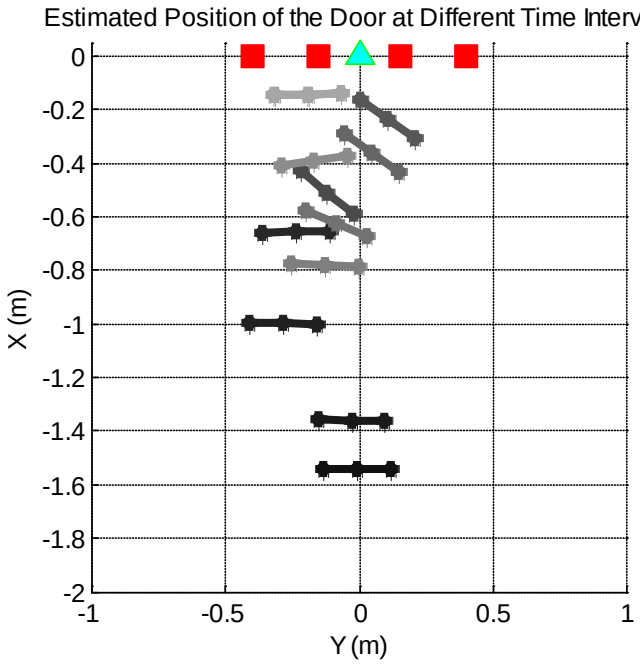

Figure 3.9: Estimated position of the door at different time intervals

Also from Figure 3.11 we can see that at the beginning of the experiment, since AMR sensors are not available yet, updates are performed only with Sonar sensors (State 1) and hence an estimate of y is not available. However as soon as AMR sensors become available ($t \cong 5.5\ sec$), estimation of y becomes possible as well.

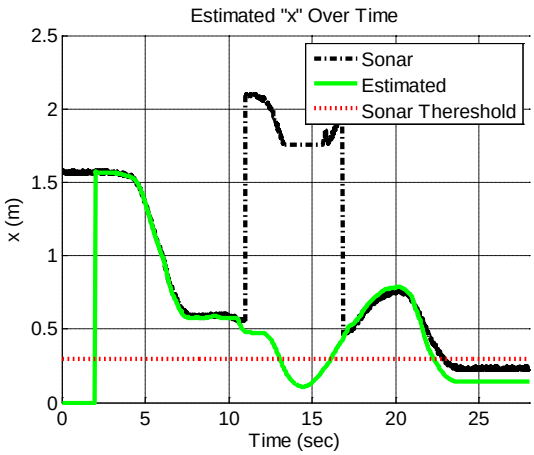

Figure 3.10: Estimated "x" over time

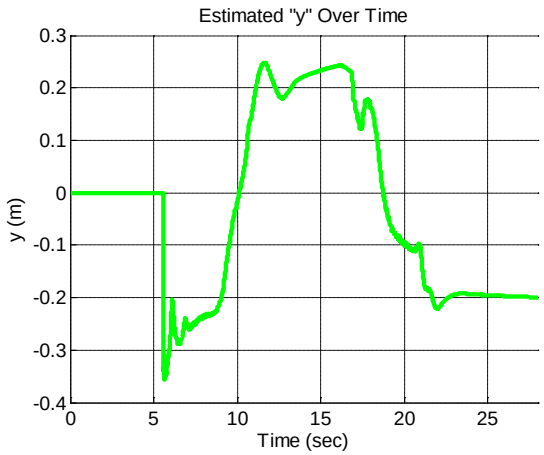

Figure 3.11: Estimated "y" over time

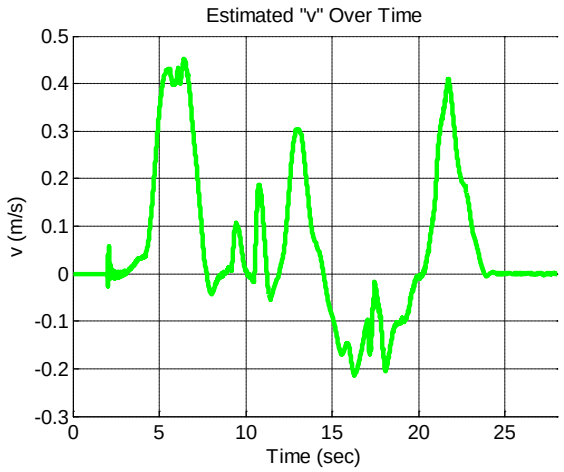

Figure 3.12: Estimated longitudinal velocity over time

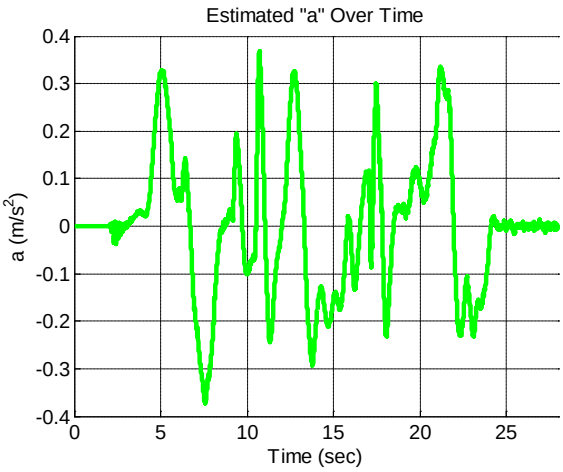

Figure 3.13: Estimated longitudinal acceleration over time

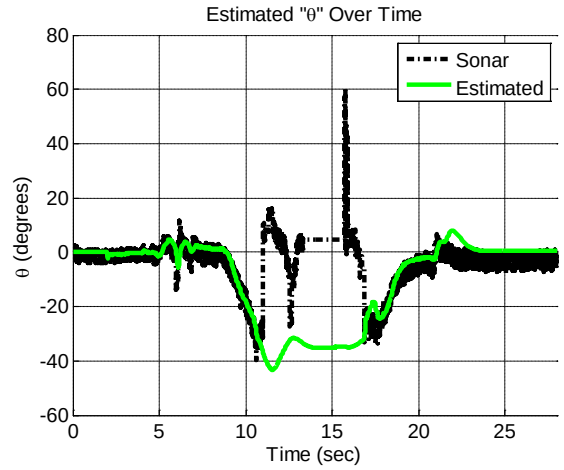

Figure 3.14: Estimated orientation over time

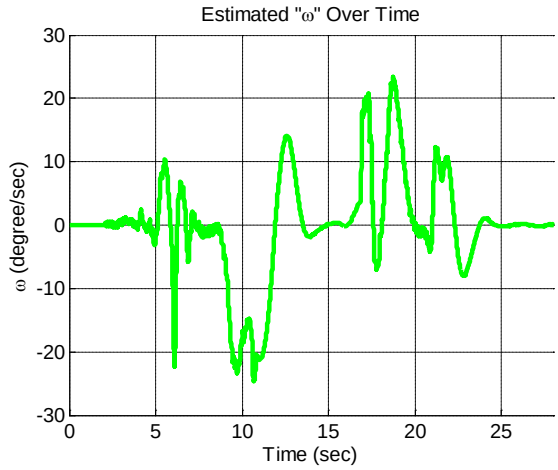

Figure 3.15: Estimated rotational velocity over time

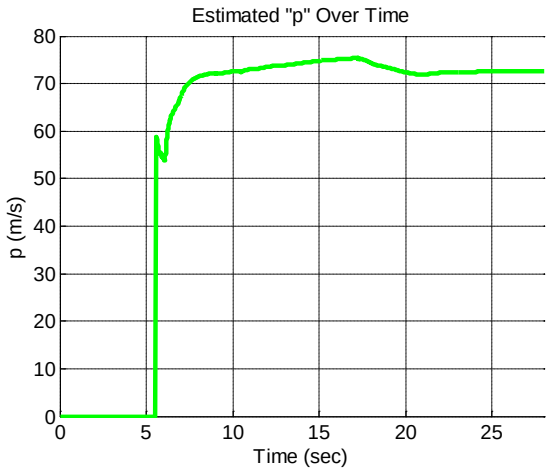

Figure 3.16: Estimated "p" over time

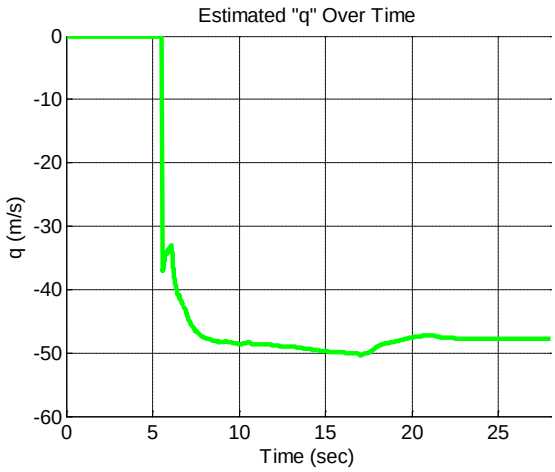

Figure 3.17: Estimated "q" over time

3.4.2 Results from Tests with the Mazda Protégé

In each test with the Mazda car, it moved toward the sensors at a fixed angle. Figures 3.18 to 3.25 show the result one of the tests when the car moved at about -20 degrees. In these figures the pink triangular indicates the time when an approaching vehicle is detected. The blue circle indicates the time when the AMR sensors are responding. Also in this test, x_{th} for the Sonar sensor has been set to 1 meter and hence the estimator switches from state 1 to 2 when $x < x_{th} = 1\ m$, However, the sonar measurements are valid up to .3 meters from the transducers. With this higher threshold we can evaluate the estimator performance by comparing sonar system and estimator values.

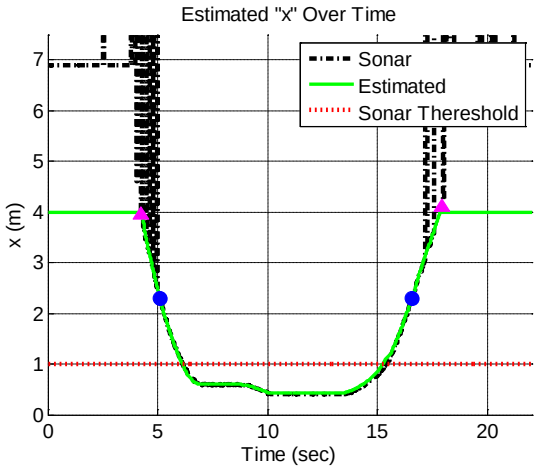

Figure 3.18: Estimated "x" over time

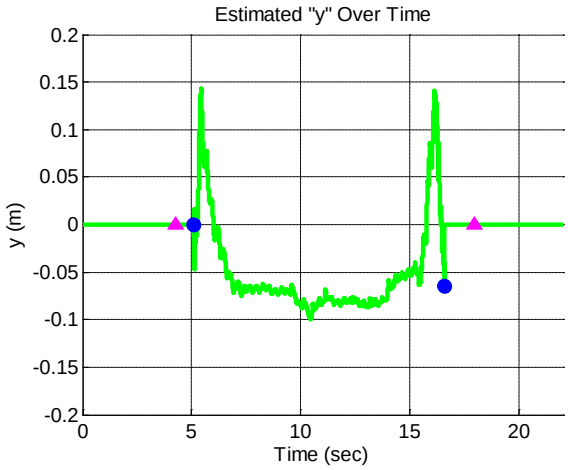

Figure 3.19: Estimated "y" over time

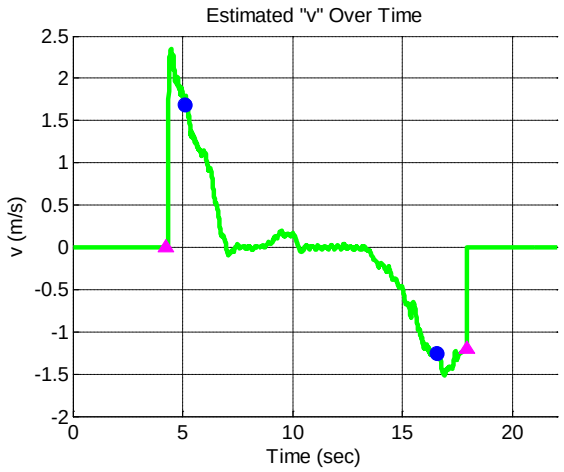

Figure 3.20: Estimated longitudinal velocity over time

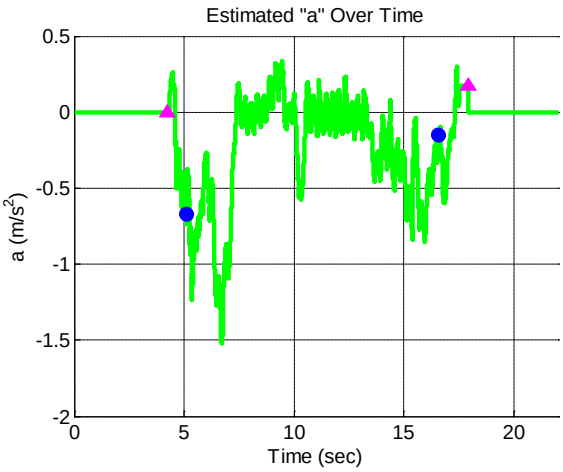

Figure 3.21: Estimated longitudinal acceleration over time

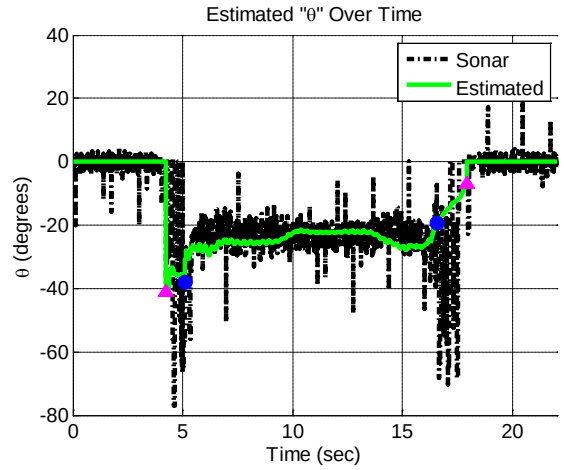

Figure 3.22: Estimated orientation over time

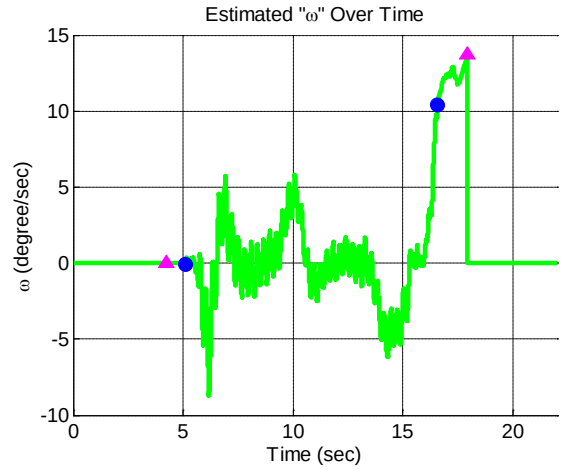

Figure 3.23: Estimated rotational velocity over time

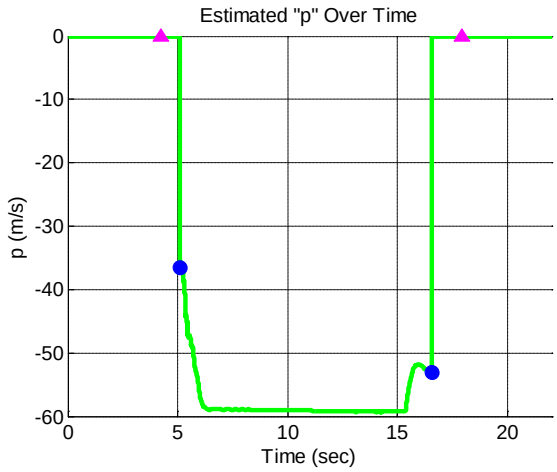

Figure 3.24: Estimated "p" over time

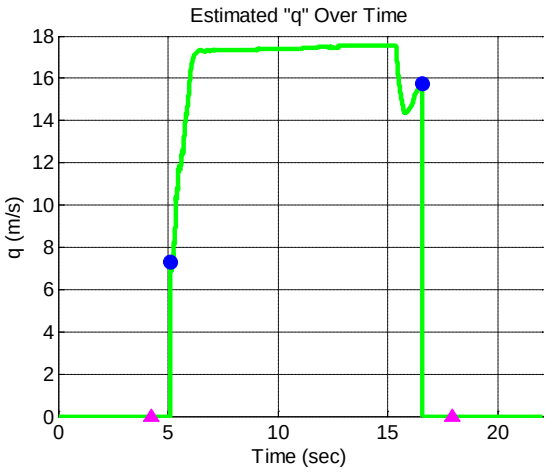

Figure 3.25: Estimated "q" over time

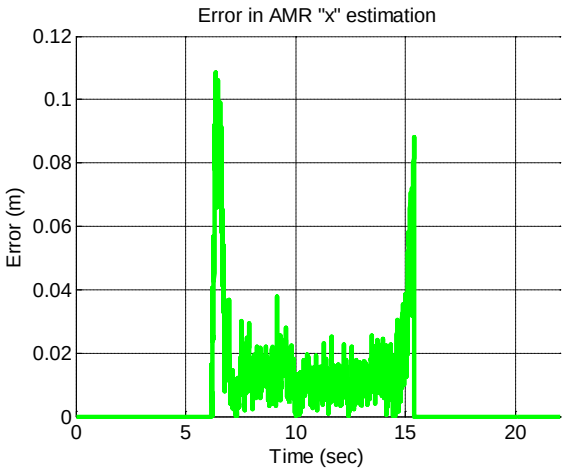

Figure 3.26: Error in estimated distance

Figure 3.26 shows the error between AMR estimation (state 2) and sonar measurement. The sonar works in distances more than .3 meters but the sonar threshold was set to 1 meter in this test for comparison.

The estimator was also verified with approaching angles up to 40 degrees and similar results were obtained. The major difference is that the approaching vehicle was detected at lower distances.

3.4.3 Test with Mazda Vehicle Moving toward Sensors at about 40 Degrees

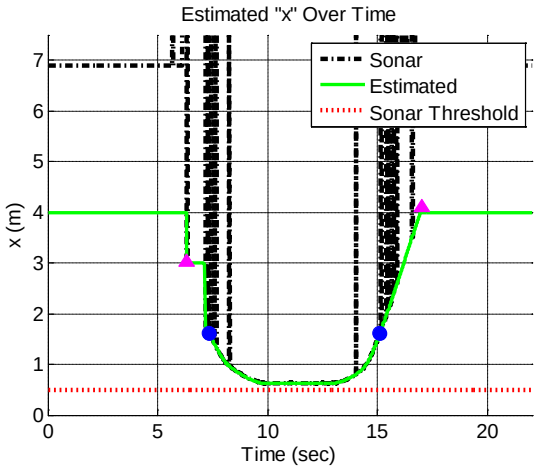

Figure 3.27: Estimated "x" over time

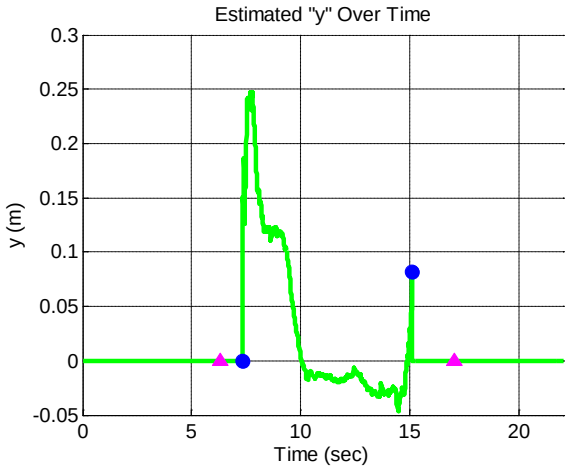

Figure 3.28: Estimated "y" over time

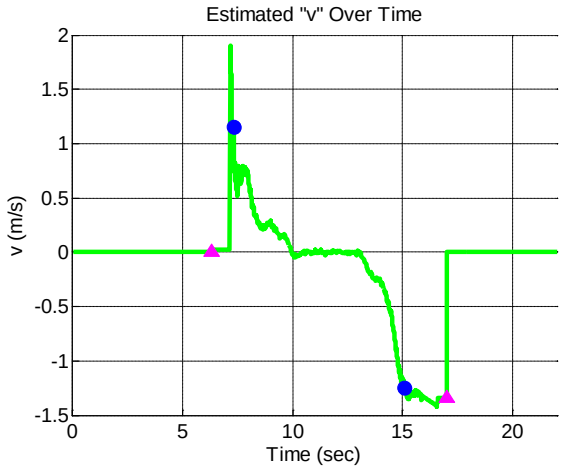

Figure 3.29: Estimated longitudinal velocity over time

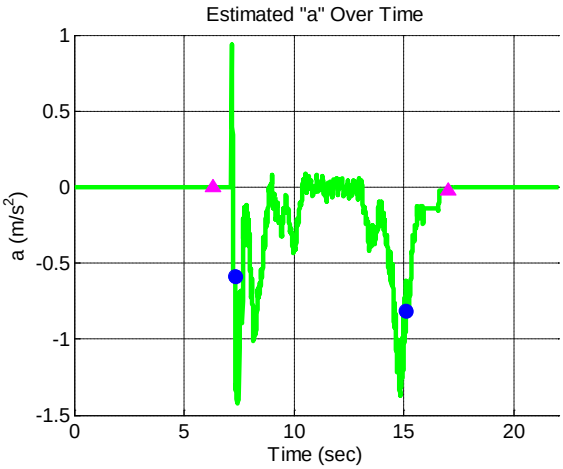

Figure 3.30: Estimated longitudinal acceleration over time

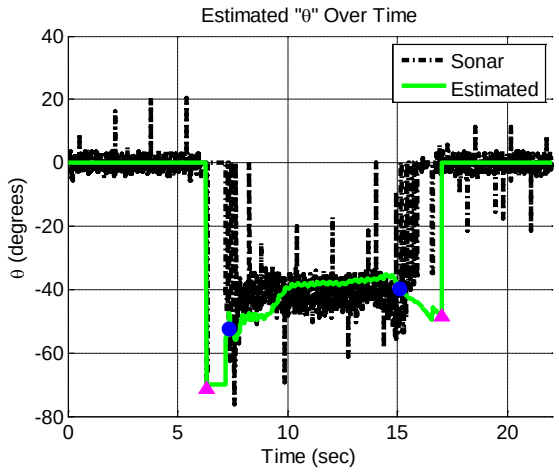

Figure 3.31: Estimated orientation over time

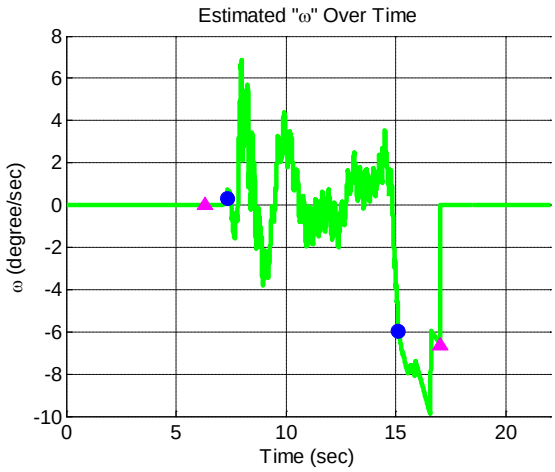

Figure 3.32: Estimated rotational velocity over time

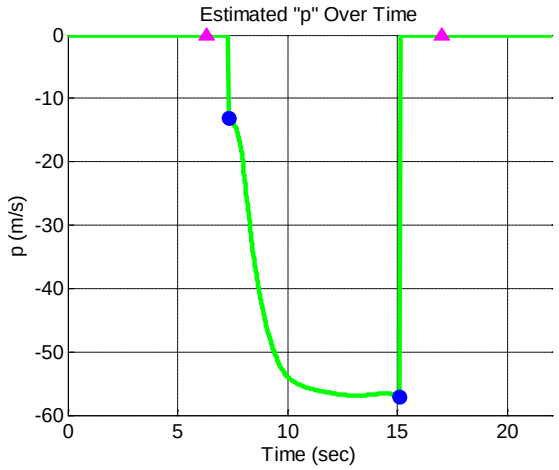

Figure 3.33: Estimated "p" over time

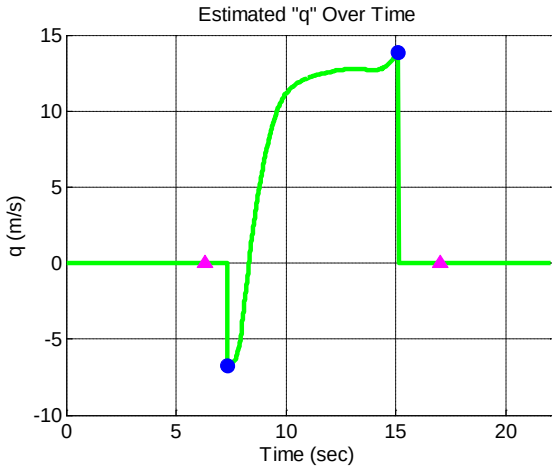

Figure 3.34: Estimated "q" over time

4 Occupant Dynamics and Occupant Protection

This chapter focuses on illustrating the potential benefits of an imminent collision detection system for enhancing occupant safety. Occupant protection measures that could be initiated when an impending collision is detected include seat belt pre-tightening, seat belt force control, seat back motion control, airbag inflation and active structural enhancement of the vehicle. This chapter utilizes seat belt pre-tightening, seat belt force control and seat back motion control to illustrate one possible tool for occupant protection. Sec 4.1 of the chapter focuses on development of a dynamic model for occupant during a front-to-back or rear-end collision. Sec 4.2 focuses on model enhancements to include friction forces, airbag forces and seat back forces. Sec 4.3 develops a lnearized model that can be used for control design. Sec 4.4. develops seat belt and seat back motion control laws and presents simulation results on the performance of these control laws.

4.1 Development of System Equations

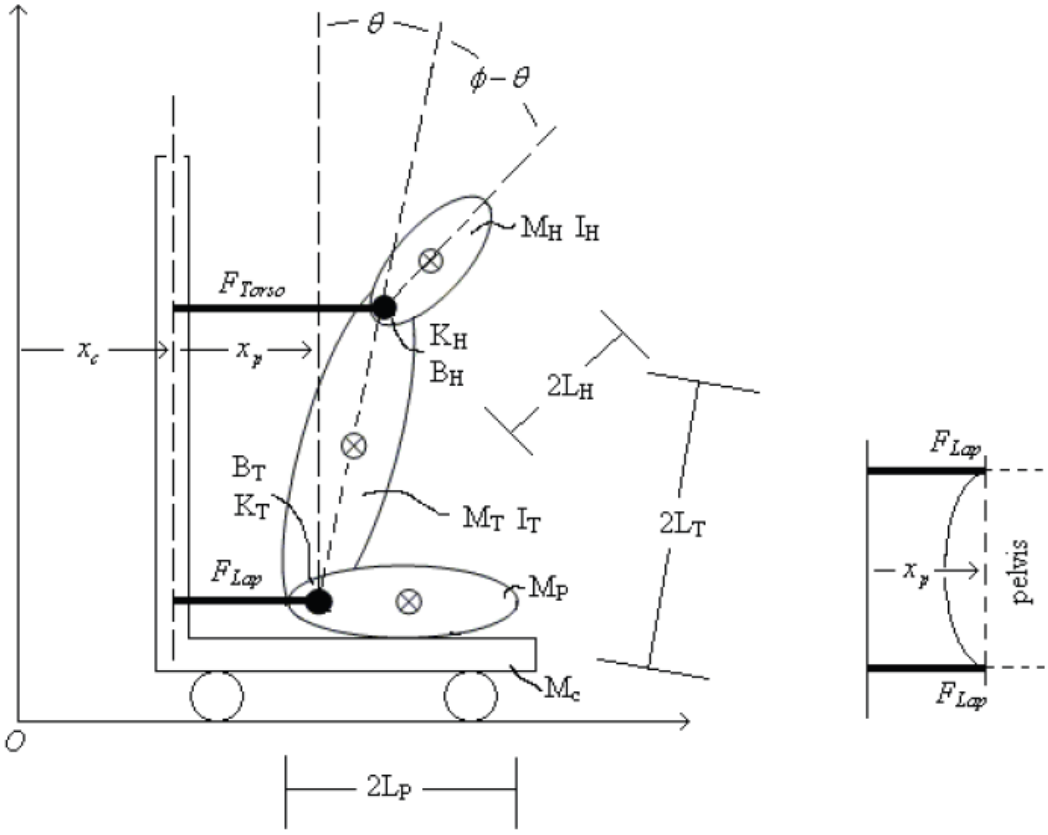

Figure 4.1: Three-Bodied Occupant Model [21]

The following variables are used in the derivation of the system equations for an occupant in a frontal collision:

$M_P - Mass\ of\ the\ pelvis, M_T - \ Mass\ of\ the\ torso, M_H - \ Mass\ of\ the\ head$

$I_T - \ Moment\ of\ inertia\ of\ the\ torso, I_H - \ Moment\ of\ inertia\ of\ the\ head$

$F_{Lap} - \ Seat\ belt\ force\ on\ the\ pelvis$

$F_{Torso} - \ Seat\ belt\ force\ on\ the\ torso$

$L_T - \ Half\ length\ of\ the\ torso, L_H - \ Half\ length\ of\ the\ head$

$x_c - \ Displacement\ of\ the\ seat\ (car)\ along\ x - axis$

$x_P - \ Displacement\ of\ the\ pelvis\ along\ x - axis$

$\theta - Rotational\ angle\ of\ the\ torso, \emptyset - Rotational\ angle\ of\ the\ head$

$K_T - \ Rotational\ spring\ coefficient\ between\ the\ pelvis\ and\ the\ torso$

$K_H - \ Rotational\ spring\ coefficient\ between\ the\ torso\ and\ the\ head$

$B_T - Rotational\ damping\ coefficient\ between\ the\ pelvis\ and\ the\ torso$

$B_H - \ Rotational\ damping\ coefficient\ between\ the\ torso\ and\ the\ head$

4.1.1 Degrees of Freedom of the System

The degrees of freedom of the system consist of the following three variables:

a) Relative motion of the pelvis with respect to the seat (translation) x_p

b) Rotational motion of the torso θ

c) Rotational motion of the neck $\emptyset$

The vector of coordinates is as follows:

$$\tilde{q} = \{q_1, q_2, q_3\} = \{x_c + x_P, \theta, \emptyset\}$$

4.1.2 Forces on the System

The generalized forces that act on the system can be written down as follows:

$\tilde{Q} = \{Q_x, Q_\theta, Q_\emptyset\}$

$$Q_x = -2F_{Lap} - F_{Torso} \tag{4.1}$$

$$Q_\theta = -2L_T F_{Torso} cos\theta - K_T\theta - B_T\dot{\theta} + K_H(\emptyset - \theta) + B_H(\dot{\emptyset} - \dot{\theta}) \quad (4.2)$$

$$Q_\emptyset = -K_H(\emptyset - \theta) - B_H(\dot{\emptyset} - \dot{\theta}) \quad (4.3)$$

4.1.3 Directions of Motion

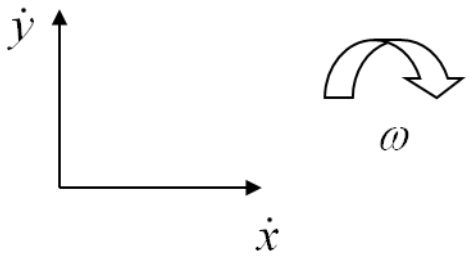

Figure 4.2: Positive directions for translation and rotation

4.1.4 Velocities of the Three Bodies along each Direction

Pelvis:

$$\dot{x}_1 = \dot{x}_c + \dot{x}_P \quad (4.4)$$

$$\dot{y}_1 = 0 \quad (4.5)$$

$$w_1 = 0 \quad (4.6)$$

Torso:

$$\dot{x}_2 = \dot{x}_c + \dot{x}_P + (L_T sin\theta)' = \dot{x}_c + \dot{x}_P + L_T\dot{\theta}cos\theta \quad (4.7)$$

$$\dot{y}_2 = (L_T cos\theta)' = -L_T\dot{\theta}sin\theta \quad (4.8)$$

$$w_2 = \dot{\theta} \quad (4.9)$$

Head:

$$\dot{x}_3 = \dot{x}_c + \dot{x}_P + (2L_T sin\theta)' + (L_H sin\emptyset)' = \dot{x}_c + \dot{x}_P + 2L_T\dot{\theta}cos\theta + L_H\dot{\emptyset}cos\emptyset \quad (4.10)$$

$$\dot{y}_3 = (2L_T cos\theta + L_H cos\emptyset)' = -2L_T\dot{\theta}sin\theta - L_T\dot{\emptyset}sin\emptyset \quad (4.11)$$

$$w_3 = \dot{\emptyset} \quad (4.12)$$

4.1.5 Energy of the Three Bodies

The sum of kinetic and potential energies for each of the 3 bodies is written down as follows:

Pelvis:

$$T_P = \frac{1}{2}M_P\left(\dot{x_1}^2 + \dot{y_1}^2\right) + \frac{1}{2}I_P{w_1}^2 = \frac{1}{2}M_P(\dot{x}_c + \dot{x}_P)^2 \quad (4.13)$$

$$U_P = 0 \quad (4.14)$$

Torso:

$$T_T = \frac{1}{2}M_T\left(\dot{x_2}^2 + \dot{y_2}^2\right) + \frac{1}{2}I_T{w_2}^2$$

$$= \frac{1}{2}M_T[\left(\dot{x}_c + \dot{x}_P + L_T\dot{\theta}cos\theta\right)^2 + (-L_T\dot{\theta}sin\theta)^2] + \frac{1}{2}I_T\dot{\theta}^2 \quad (4.15)$$

$$U_P = M_T g L_T cos\theta \quad (4.16)$$

Head:

$$T_H = \frac{1}{2}M_H\left(\dot{x_3}^2 + \dot{y_3}^2\right) + \frac{1}{2}I_H{w_3}^2$$

$$= \frac{1}{2}M_H[(\dot{x}_c + \dot{x}_P + 2L_T\dot{\theta}cos\theta + L_H\dot{\emptyset}cos\emptyset)^2 + (-2L_T\dot{\theta}sin\theta - L_T\dot{\emptyset}sin\emptyset)^2]$$

$$+ \frac{1}{2}I_H\dot{\emptyset}^2 \quad (4.17)$$

$$U_H = M_H g(2L_T cos\theta + L_H cos\emptyset) \tag{4.18}$$

4.1.6 Lagrangian Equations

Using the Lagrangian

$$L = T - U = (T_P + T_T + T_H) - (U_P + U_T + U_H) \tag{4.19}$$

and

$$\frac{d}{dt}\left(\frac{\partial L}{\partial \dot{q}_i}\right) - \left(\frac{\partial L}{\partial q_i}\right) = Q_i \tag{4.20}$$

the following three equations of motion are obtained:

$$\frac{d}{dt}\left(\frac{\partial L}{\partial \dot{q}_1}\right) - \left(\frac{\partial L}{\partial q_1}\right) = \frac{d}{dt}\left(\frac{\partial L}{\partial(\dot{x}_c + \dot{x}_P)}\right) - \left(\frac{\partial L}{\partial(x_c + x_P)}\right) = Q_x \tag{4.21}$$

$$\frac{d}{dt}\left(\frac{\partial L}{\partial \dot{q}_2}\right) - \left(\frac{\partial L}{\partial q_2}\right) = \frac{d}{dt}\left(\frac{\partial L}{\partial \dot{\theta}}\right) - \left(\frac{\partial L}{\partial \theta}\right) = Q_\theta \tag{4.22}$$

$$\frac{d}{dt}\left(\frac{\partial L}{\partial \dot{q}_3}\right) - \left(\frac{\partial L}{\partial q_3}\right) = \frac{d}{dt}\left(\frac{\partial L}{\partial \dot{\emptyset}}\right) - \left(\frac{\partial L}{\partial \emptyset}\right) = Q_\emptyset \tag{4.23}$$

4.1.7 Final Results

Substituting of the expression of L and simplifying the equations, the final forms of equations of motions are:

$$M_1(\ddot{x}_c + \ddot{x}_P) + M_2 L_T\left(\ddot{\theta} cos\theta - \dot{\theta}^2 sin\theta\right) + M_3 L_H\left(\ddot{\emptyset} cos\emptyset - \dot{\emptyset}^2 sin\emptyset\right) = Q_x \tag{4.24}$$

$$\begin{aligned} M_2 L_T(\ddot{x}_c + \ddot{x}_P)cos\theta + [(M_2 + 2M_3){L_T}^2 + I_T]\ddot{\theta} \\ + M_3(2L_T L_H)\left(\ddot{\emptyset}\cos(\emptyset - \theta) - \dot{\emptyset}^2 \sin(\emptyset - \theta)\right) - M_2 g L_T sin\theta \\ = Q_\theta \end{aligned} \tag{4.25}$$

$$M_3 L_H(\ddot{x}_c + \ddot{x}_P)cos\emptyset + \left(M_3 {L_H}^2 + I_H\right)\ddot{\emptyset} + M_3(2L_T L_H)\left(\ddot{\theta}\cos(\emptyset - \theta) + \dot{\theta}^2 \sin(\emptyset - \theta)\right) - M_3 g L_H sin\emptyset = Q_\emptyset \quad (4.26)$$

where:

$$M_1 = M_P + M_T + M_H$$

$$M_2 = M_T + 2M_H$$

$$M_3 = M_H$$

$$Q_x = -2F_{Lap} - F_{Torso}$$

$$Q_\theta = -2L_T F_{Torso} cos\theta - K_T\theta - B_T\dot{\theta} + K_H(\emptyset - \theta) + B_H(\dot{\emptyset} - \dot{\theta})$$

and

$$Q_\emptyset = -K_H(\emptyset - \theta) - B_H(\dot{\emptyset} - \dot{\theta}).$$

4.1.8 Paulitz's Results

These equations can be compared to those in Paulitz [15]:

$$M_1(\ddot{x}_c + \ddot{x}_P) + M_2 L_T\left(\ddot{\theta}cos\theta - \dot{\theta}^2 sin\theta\right) + M_3 L_H\left(\ddot{\emptyset}cos\emptyset - \dot{\emptyset}^2 sin\emptyset\right) = -Q_x \quad (4.27)$$

$$M_2 L_T(\ddot{x}_c + \ddot{x}_P)cos\theta + (M_3(2L_T)^2 + I_T)\ddot{\theta} + M_3(2L_T L_H)\left(\ddot{\emptyset}\cos(\emptyset - \theta) - \dot{\emptyset}^2 \sin(\emptyset - \theta)\right) - M_2 g L_T sin\theta = -Q_\theta \quad (4.28)$$

$$M_3 L_H(\ddot{x}_c + \ddot{x}_P)cos\emptyset + I_H\ddot{\emptyset} + M_3(2L_T L_H)\left(\ddot{\theta}\cos(\emptyset - \theta) + \dot{\theta}^2 \sin(\emptyset - \theta)\right) - M_3 g L_H sin\emptyset = -Q_\emptyset \quad (4.29)$$

where:

$$M_1 = M_P + M_T + M_H$$

$$M_2 = M_T + 2M_H$$

$$M_3 = M_H$$

$$Q_x = 2F_{Lap} + F_{Torso}$$

$$Q_\theta = 2L_T F_{Torso} cos\theta + K_T\theta + B_T\dot{\theta} - K_H(\emptyset - \theta) - B_H(\dot{\emptyset} - \dot{\theta})$$

$$Q_\emptyset = K_H(\emptyset - \theta) + B_H(\dot{\emptyset} - \dot{\theta})$$

4.1.9 Discrepancies of Equations

Two discrepancies exist between our derivation and Paulitz's results.

a) Second term of the second equation

In Eq. (4.25), the second term is $[(M_2 + 2M_3){L_T}^2 + I_T]\ddot{\theta}$ where as in Eq. (4.28), the second term is $(M_3(2L_T)^2 + I_T)\ddot{\theta}$.

Substituting in $M_2 = M_T + 2M_H$ and $M_3 = M_H$:

$$\left[(M_2 + 2M_3){L_T}^2 + I_T\right]\ddot{\theta} = M_2{L_T}^2\ddot{\theta} + 4M_3{L_T}^2\ddot{\theta} + I_T\ddot{\theta}$$

$$(M_3(2L_T)^2 + I_T)\ddot{\theta} = 4M_3{L_T}^2\ddot{\theta} + I_T\ddot{\theta}$$

There is an extra term $M_2{L_T}^2\ddot{\theta}$ in the second equation of our derivation.

b) Second term of the third equation

In Eq. (4.26), the second term is $\left(M_3{L_H}^2 + I_H\right)\ddot{\emptyset}$ where as in Eq. (4.9), the second term is $I_H\ddot{\emptyset}$. There is an extra term $M_3{L_H}^2\ddot{\emptyset}$ in the second equation of our derivation.

Based on intuitive considerations, our final equations seem more accurate than those of Paulitz and are therefore assumed to be correct.

4.2 Model Enhancement

4.2.1 Addition of Friction

When dry friction is present between the seat and the body, a friction term F_f must be added to Eq. (4.1) of the model. Eq. (4.1) becomes

$$M_1(\ddot{x}_c + \ddot{x}_P) + M_2L_T\left(\ddot{\theta}cos\theta - \dot{\theta}^2sin\theta\right) + M_3L_H\left(\ddot{\emptyset}cos\emptyset - \dot{\emptyset}^2sin\emptyset\right) = -2F_{Lap} - F_{Torso} + F_f \quad (4.30)$$

The friction term depends on the relative velocity $\dot{x}_P$ between the pelvis and the seat.

a) If $\dot{x}_P > 0$, $F_f = -f_0$ (4.31)

b) If $\dot{x}_P < 0$, $F_f = f_0$ (4.32)

c) If $\dot{x}_P = 0$ and $f_0 > \left|M_1\ddot{x}_c + M_2L_T\left(\ddot{\theta}cos\theta - \dot{\theta}^2sin\theta\right) + M_3L_H\left(\ddot{\emptyset}cos\emptyset - \dot{\emptyset}^2sin\emptyset\right) + +2F_{Lap} + F_{Torso}\right|$, then

$$F_f = M_1\ddot{x}_c + M_2L_T\left(\ddot{\theta}cos\theta - \dot{\theta}^2sin\theta\right) + M_3L_H\left(\ddot{\emptyset}cos\emptyset - \dot{\emptyset}^2sin\emptyset\right) + 2F_{Lap} + F_{Torso} \quad (4.33)$$

d) If $\dot{x}_P = 0$ and $f_0 \leq \left|M_1\ddot{x}_c + M_2L_T\left(\ddot{\theta}cos\theta - \dot{\theta}^2sin\theta\right) + M_3L_H\left(\ddot{\emptyset}cos\emptyset - \dot{\emptyset}^2sin\emptyset\right) + +2F_{Lap} + F_{Torso}\right|$, then

$$F_f = 0 \quad (4.34)$$

4.2.2 Addition of Airbag Forces F_{ABH} and F_{ABT}

The presence of a frontal airbag is modeled as exerting equivalent forces at one point each on the torso and the head. These forces are denoted as F_{ABT} and F_{ABH} respectively in Figure 4.3.

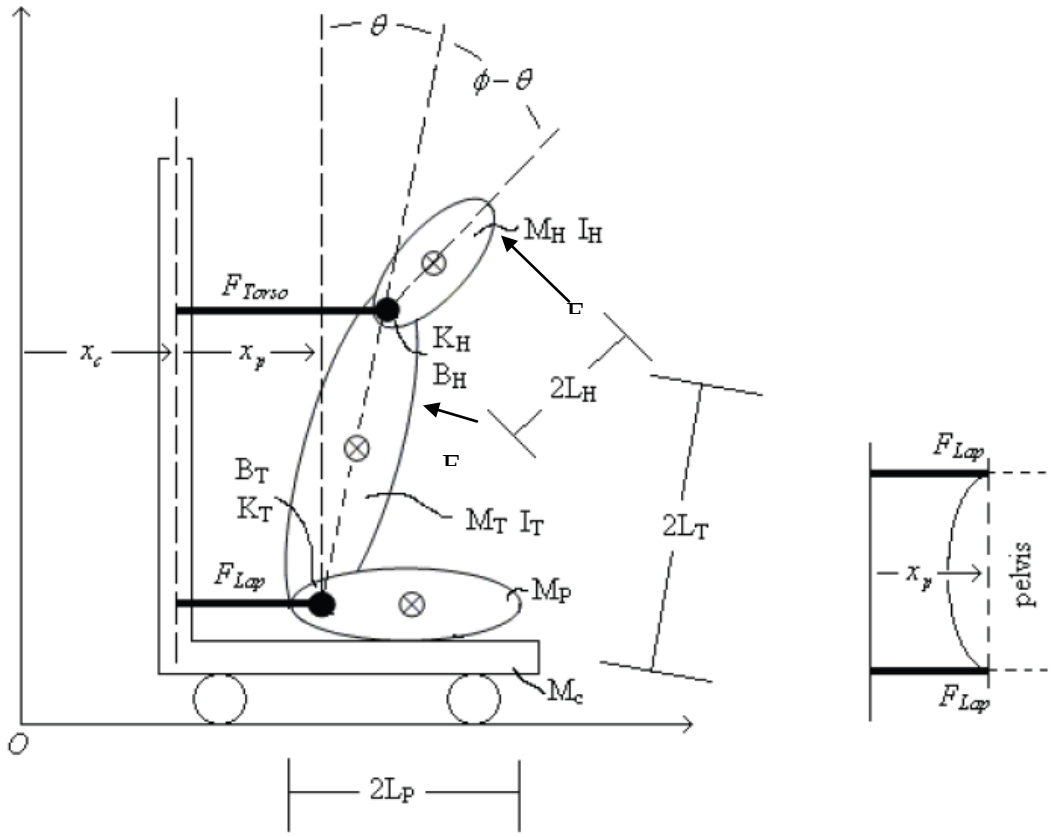

Figure 4.3: Occupant dynamics with airbag forces on torso and head

The original equations (4.24), (4.25) and (4.26) still hold:

$$M_1(\ddot{x}_c + \ddot{x}_P) + M_2 L_T\left(\ddot{\theta}cos\theta - \dot{\theta}^2 sin\theta\right) + M_3 L_H\left(\ddot{\emptyset}cos\emptyset - \dot{\emptyset}^2 sin\emptyset\right) = Q_x$$

$$M_2 L_T(\ddot{x}_c + \ddot{x}_P)cos\theta + [(M_2 + 2M_3){L_T}^2 + I_T]\ddot{\theta} + M_3(2L_T L_H)\left(\ddot{\emptyset}\cos(\emptyset - \theta) - \dot{\emptyset}^2 \sin(\emptyset - \theta)\right) - M_2 g L_T sin\theta = Q_\theta$$

$$M_3 L_H(\ddot{x}_c + \ddot{x}_P)cos\emptyset + \left(M_3{L_H}^2 + I_H\right)\ddot{\emptyset} + M_3(2L_T L_H)\left(\ddot{\theta}\cos(\emptyset - \theta) + \dot{\theta}^2 \sin(\emptyset - \theta)\right) - M_3 g L_H sin\emptyset = Q_\emptyset$$

But the forces change to:

$$Q_x = -2F_{Lap} - F_{Torso} + F_f - F_{ABT}\cos\theta - F_{ABH}\cos\emptyset \qquad (4.35)$$

$$Q_\theta = -2L_T F_{Torso} cos\theta - K_T\theta - B_T\dot{\theta} + K_H(\emptyset - \theta) + B_H\left(\dot{\emptyset} - \dot{\theta}\right) - 2L_{ABT}F_{ABT} \quad (4.36)$$

$$Q_\emptyset = -K_H(\emptyset - \theta) - B_H\left(\dot{\emptyset} - \dot{\theta}\right) - 2L_H F_{ABH} \quad (4.37)$$

The airbag forces on the torso and on the head are given by

If $2L_{ABT}\theta < L_{ABT\_contact},\ F_{ABT} = 0$

Otherwise $F_{ABT} = K_{AB}(2L_{ABT}\theta - L_{ABT\_contact})$ (4.38)

If $2L_T\theta + 2L_H(\emptyset - \theta) < L_{ABH\_contact},\ F_{ABH} = 0$

Otherwise $F_{ABH} = K_{AB}(2L_T\theta + 2L_H\emptyset - 2L_H\theta - L_{ABH\_contact})$ (4.39)

4.2.3 Addition of Seat Back Forces

It is important to model the forces due to the seat back, since the seat back is the only object that exerts resistive forces on the occupant body when the occupant is moving in a direction away from the steering wheel. The seat back is modeled as applying forces F_{seat_lap} and F_{seat_torso} at two points, one each on the lap and the torso respectively.

Seat force *F_seat_lap* will be in effect when $x_p < 0$

and *F_seat_torso* will be in effect when $x_{torso} = x_p + L_T \sin\theta < 0$

On adding seat force terms, the generalized forces become

$$Q_x = -2F_{Lap} - F_{Torso} + F_{seat\ lap} + F_{seat\ torso} + F_f - F_{ABT}\cos\theta - F_{ABH}\cos\emptyset \quad (4.40)$$

$$Q_\theta = -2L_T F_{Torso} cos\theta + 2L_T F_{seat\ torso} cos\theta - K_T\theta - B_T\dot{\theta} + K_H(\emptyset - \theta) + B_H\left(\dot{\emptyset} - \dot{\theta}\right) - 2L_{ABT}F_{ABT} \quad (4.41)$$

$$Q_\emptyset = -K_H(\emptyset - \theta) - B_H\left(\dot{\emptyset} - \dot{\theta}\right) - 2L_H F_{ABH} \quad (4.42)$$

Seat force profiles:

The seat back is modeled as having a stiffening set of springs and dampers. The spring

coefficients are K_{seat} and K_{seat_max} for seat back displacements less than 0.02 meters and higher than 0.02 meters respectively. The corresponding damping coefficients are assumed to be B_{seat} and B_{seat_max}.

F_seat_lap:

If ($x_p < 0$ and $x_p > -0.02$)

$$F_{seat\ lap} = -K_{seat} * x_p - B_{seat} * \dot{x}_p$$

If ($x_p < -0.02$ and $x_p > -0.03$)

$$K_{temp\ lap} = K_{seat} + (K_{seat} - K_{seat\ max}) * (x_p + 0.02)/0.01$$

$$B_{temp\ lap} = B_{seat} + (B_{seat} - B_{seat\ max}) * (x_p + 0.02)/0.01$$

$$F_{seat\ lap} = -K_{temp\ lap} * x_p - B_{temp\ lap} * \dot{x}_p$$

If ($x_p < -0.03$)

$$F_{seat\ lap} = -K_{seat\ max} * x_p - B_{seat\ max} * \dot{x}_p$$

(4.43)

F_seat_torso:

If ($x_{torso} < 0$ and $x_{torso} > -0.02$)

$$F_{seat\ torso} = -K_{seat} * x_{torso} - B_{seat} * \dot{x}_{torso}$$

If ($x_{torso} < -0.02$ and $x_{torso} > -0.03$)

$$K_{temp\ torso} = K_{seat} + (K_{seat} - K_{seat\ max}) * (x_{torso} + 0.02)/0.01$$

$$B_{temp\ torso} = B_{seat} + (B_{seat} - B_{seat\ max}) * (x_{torso} + 0.02)/0.01$$

$$F_{seat\ torso} = -K_{temp\ torso} * x_{torso} - B_{temp\ torso} * \dot{x}_{torso}$$

If ($x_{torso} < -0.03$)

$$F_{seat\ torso} = -K_{seat\ max} * x_{torso} - B_{seat\ max} * \dot{x}_{torso}$$

(4.44)

4.3 Model Linearization

4.3.1 Matrix Form Representation

In matrix form, $\ddot{x}_P, \ddot{\theta}, \ddot{\emptyset}$ can be represented as:

$$\begin{bmatrix} M_1 & M_2L_T cos\theta & M_3L_H cos\emptyset \\ M_2L_T cos\theta & (M_2+2M_3){L_T}^2 + I_T & M_3(2L_TL_H)\cos(\emptyset-\theta) \\ M_3L_H cos\emptyset & M_3(2L_TL_H)\cos(\emptyset-\theta) & \left(M_3{L_H}^2 + I_H\right) \end{bmatrix} \begin{bmatrix} \ddot{x}_P \\ \ddot{\theta} \\ \ddot{\emptyset} \end{bmatrix} = \begin{bmatrix} Q_x + F_f - M_1\ddot{x}_c + M_2L_T\dot{\theta}^2 sin\theta + M_3L_H\dot{\emptyset}^2 sin\emptyset \\ Q_\theta - M_2L_T\ddot{x}_c cos\theta + M_3(2L_TL_H)\dot{\emptyset}^2\sin(\emptyset-\theta) + M_2gL_T sin\theta \\ Q_\emptyset - M_3L_H\ddot{x}_c cos\emptyset - M_3(2L_TL_H)\dot{\theta}^2\sin(\emptyset-\theta) + M_3gL_H sin\emptyset \end{bmatrix} \tag{4.45}$$

Thus:

$$\begin{bmatrix} \ddot{x}_P \\ \ddot{\theta} \\ \ddot{\emptyset} \end{bmatrix} = \begin{bmatrix} M_1 & M_2L_T cos\theta & M_3L_H cos\emptyset \\ M_2L_T cos\theta & (M_2+2M_3){L_T}^2 + I_T & M_3(2L_TL_H)\cos(\emptyset-\theta) \\ M_3L_H cos\emptyset & M_3(2L_TL_H)\cos(\emptyset-\theta) & \left(M_3{L_H}^2 + I_H\right) \end{bmatrix}^{-1} * \begin{bmatrix} Q_x + F_f - M_1\ddot{x}_c + M_2L_T\dot{\theta}^2 sin\theta + M_3L_H\dot{\emptyset}^2 sin\emptyset \\ Q_\theta - M_2L_T\ddot{x}_c cos\theta + M_3(2L_TL_H)\dot{\emptyset}^2\sin(\emptyset-\theta) + M_2gL_T sin\theta \\ Q_\emptyset - M_3L_H\ddot{x}_c cos\emptyset - M_3(2L_TL_H)\dot{\theta}^2\sin(\emptyset-\theta) + M_3gL_H sin\emptyset \end{bmatrix} \tag{4.46}$$

4.3.2 Linearization of the Matrix Form

In order to implement LQR design, the matrix needs to be linearized. Start with the matrix form:

$$\begin{bmatrix} M_1 & M_2L_T cos\theta & M_3L_H cos\emptyset \\ M_2L_T cos\theta & (M_2+2M_3){L_T}^2 + I_T & M_3(2L_TL_H)\cos(\emptyset-\theta) \\ M_3L_H cos\emptyset & M_3(2L_TL_H)\cos(\emptyset-\theta) & \left(M_3{L_H}^2 + I_H\right) \end{bmatrix} \begin{bmatrix} \ddot{x}_P \\ \ddot{\theta} \\ \ddot{\emptyset} \end{bmatrix} = \begin{bmatrix} Q_x + F_f - M_1\ddot{x}_c + M_2L_T\dot{\theta}^2 sin\theta + M_3L_H\dot{\emptyset}^2 sin\emptyset \\ Q_\theta - M_2L_T\ddot{x}_c cos\theta + M_3(2L_TL_H)\dot{\emptyset}^2\sin(\emptyset-\theta) + M_2gL_T sin\theta \\ Q_\emptyset - M_3L_H\ddot{x}_c cos\emptyset - M_3(2L_TL_H)\dot{\theta}^2\sin(\emptyset-\theta) + M_3gL_H sin\emptyset \end{bmatrix}$$

with

$$M_1 = M_P + M_T + M_H$$

$$M_2 = M_T + 2M_H$$

$$M_3 = M_H$$

$$Q_x = -2F_{Lap} - F_{Torso}$$

$$Q_\theta = -2L_T F_{Torso} cos\theta - K_T\theta - B_T\dot{\theta} + K_H(\emptyset - \theta) + B_H(\dot{\emptyset} - \dot{\theta})$$

$$Q_\emptyset = -K_H(\emptyset - \theta) - B_H(\dot{\emptyset} - \dot{\theta})$$

Linearize the matrix on the left side:

$$\begin{bmatrix} M_1 & M_2 L_T cos\theta & M_3 L_H cos\emptyset \\ M_2 L_T cos\theta & (M_2 + 2M_3){L_T}^2 + I_T & M_3(2L_T L_H)\cos(\emptyset - \theta) \\ M_3 L_H cos\emptyset & M_3(2L_T L_H)\cos(\emptyset - \theta) & \left(M_3 {L_H}^2 + I_H\right) \end{bmatrix}$$
$$= \begin{bmatrix} M_1 & M_2 L_T & M_3 L_H \\ M_2 L_T & (M_2 + 2M_3){L_T}^2 + I_T & M_3(2L_T L_H) \\ M_3 L_H & M_3(2L_T L_H) & \left(M_3 {L_H}^2 + I_H\right) \end{bmatrix}$$

Linearize the matrix on the right side:

$$\begin{bmatrix} Q_x + F_f - M_1\ddot{x}_c + M_2 L_T\dot{\theta}^2 sin\theta + M_3 L_H\dot{\emptyset}^2 sin\emptyset \\ Q_\theta - M_2 L_T\ddot{x}_c cos\theta + M_3(2L_T L_H)\dot{\emptyset}^2\sin(\emptyset - \theta) + M_2 g L_T sin\theta \\ Q_\emptyset - M_3 L_H\ddot{x}_c cos\emptyset - M_3(2L_T L_H)\dot{\theta}^2\sin(\emptyset - \theta) + M_3 g L_H sin\emptyset \end{bmatrix}$$
$$= \begin{bmatrix} -2F_{Lap} - F_{Torso} + F_f - M_1\ddot{x}_c \\ -2L_T F_{Torso} - K_T\theta - B_T\dot{\theta} + K_H(\emptyset - \theta) + B_H\left(\dot{\emptyset} - \dot{\theta}\right) - M_2 L_T\ddot{x}_c + M_2 g L_T\theta \\ -K_H(\emptyset - \theta) - B_H\left(\dot{\emptyset} - \dot{\theta}\right) - M_3 L_H\ddot{x}_c + M_3 g L_H\emptyset \end{bmatrix}$$

Thus after linearization

$$\begin{bmatrix} M_1 & M_2 L_T & M_3 L_H \\ M_2 L_T & (M_2 + 2M_3){L_T}^2 + I_T & M_3(2L_T L_H) \\ M_3 L_H & M_3(2L_T L_H) & \left(M_3 {L_H}^2 + I_H\right) \end{bmatrix} \begin{bmatrix} \ddot{x}_P \\ \ddot{\theta} \\ \ddot{\emptyset} \end{bmatrix}$$
$$= \begin{bmatrix} -2F_{Lap} - F_{Torso} + F_f - M_1\ddot{x}_c \\ -2L_T F_{Torso} - K_T\theta - B_T\dot{\theta} + K_H(\emptyset - \theta) + B_H\left(\dot{\emptyset} - \dot{\theta}\right) - M_2 L_T\ddot{x}_c + M_2 g L_T\theta \\ -K_H(\emptyset - \theta) - B_H\left(\dot{\emptyset} - \dot{\theta}\right) - M_3 L_H\ddot{x}_c + M_3 g L_H\emptyset \end{bmatrix}$$

$$\begin{bmatrix} \ddot{x}_P \\ \ddot{\theta} \\ \ddot{\emptyset} \end{bmatrix} = \begin{bmatrix} M_1 & M_2 L_T & M_3 L_H \\ M_2 L_T & (M_2 + 2M_3){L_T}^2 + I_T & M_3(2L_T L_H) \\ M_3 L_H & M_3(2L_T L_H) & \left(M_3 {L_H}^2 + I_H\right) \end{bmatrix}^{-1}$$
$$* \begin{bmatrix} -2F_{Lap} - F_{Torso} + F_f - M_1\ddot{x}_c \\ -2L_T F_{Torso} - K_T\theta - B_T\dot{\theta} + K_H(\emptyset - \theta) + B_H\left(\dot{\emptyset} - \dot{\theta}\right) - M_2 L_T\ddot{x}_c + M_2 g L_T\theta \\ -K_H(\emptyset - \theta) - B_H\left(\dot{\emptyset} - \dot{\theta}\right) - M_3 L_H\ddot{x}_c + M_3 g L_H\emptyset \end{bmatrix}$$

Thus

$$\begin{bmatrix} \ddot{x}_P \\ \ddot{\theta} \\ \ddot{\emptyset} \end{bmatrix} = \begin{bmatrix} A_1 & A_2 & A_3 \\ A_4 & A_5 & A_6 \\ A_7 & A_8 & A_9 \end{bmatrix} * \begin{bmatrix} -2F_{Lap} - F_{Torso} + F_f - M_1\ddot{x}_c \\ -2L_T F_{Torso} - K_T\theta - B_T\dot{\theta} + K_H(\emptyset - \theta) + B_H(\dot{\emptyset} - \dot{\theta}) - M_2 L_T \ddot{x}_c + M_2 g L_T \theta \\ -K_H(\emptyset - \theta) - B_H(\dot{\emptyset} - \dot{\theta}) - M_3 L_H \ddot{x}_c + M_3 g L_H \emptyset \end{bmatrix}$$

(4.47)

where

$$\begin{bmatrix} A_1 & A_2 & A_3 \\ A_4 & A_5 & A_6 \\ A_7 & A_8 & A_9 \end{bmatrix} = \begin{bmatrix} M_1 & M_2 L_T & M_3 L_H \\ M_2 L_T & (M_2 + 2M_3){L_T}^2 + I_T & M_3(2L_T L_H) \\ M_3 L_H & M_3(2L_T L_H) & \left(M_3 {L_H}^2 + I_H\right) \end{bmatrix}^{-1}$$

(4.48)

Represent results in state space form as

$$\begin{bmatrix} \dot{x}_p \\ \ddot{x}_p \\ \dot{\theta} \\ \ddot{\theta} \\ \dot{\emptyset} \\ \ddot{\emptyset} \end{bmatrix} = \begin{bmatrix} 0 & 1 & 0 & 0 & 0 & 0 \\ 0 & 0 & A_2(-K_T - K_H + M_2 g L_T) + A_3 K_H & -A_2(B_T + B_H) + A_3 B_H & A_2 K_H + A_3(M_3 g L_H - K_H) & A_2 B_H - A_3 B_H \\ 0 & 0 & 0 & 1 & 0 & 0 \\ 0 & 0 & A_5(-K_T - K_H + M_2 g L_T) + A_6 K_H & -A_5(B_T + B_H) + A_6 B_H & A_5 K_H + A_6(M_3 g L_H - K_H) & A_5 B_H - A_6 B_H \\ 0 & 0 & 0 & 0 & 0 & 1 \\ 0 & 0 & A_8(-K_T - K_H + M_2 g L_T) + A_9 K_H & -A_8(B_T + B_H) + A_9 B_H & A_8 K_H + A_9(M_3 g L_H - K_H) & A_8 B_H - A_9 B_H \end{bmatrix} \begin{bmatrix} x_p \\ \dot{x}_p \\ \theta \\ \dot{\theta} \\ \emptyset \\ \dot{\emptyset} \end{bmatrix}$$
$$+ \begin{bmatrix} 0 \\ A_1(-2F_{Lap} - F_{Torso} + F_f - M_1 \ddot{x}_c) - A_2(2L_T F_{Torso} + M_2 L_T \ddot{x}_c) - A_3 M_3 L_H \ddot{x}_c \\ 0 \\ A_4(-2F_{Lap} - F_{Torso} + F_f - M_1 \ddot{x}_c) - A_5(2L_T F_{Torso} + M_2 L_T \ddot{x}_c) - A_6 M_3 L_H \ddot{x}_c \\ 0 \\ A_7(-2F_{Lap} - F_{Torso} + F_f - M_1 \ddot{x}_c) - A_8(2L_T F_{Torso} + M_2 L_T \ddot{x}_c) - A_9 M_3 L_H \ddot{x}_c \end{bmatrix} \quad (4.49)$$

The linearized model can be used for determining the feedback coefficient K by LQR design or other control design techniques that require a linear system model.

4.4 Seat Belt Control Laws

A driver involved in an accidental collision is less likely to sustain injury if the restraining forces provided by the seatbelt are regulated using an intelligent control strategy. Simple, intuitive control laws can be implemented to prevent the driver from colliding with the steering wheel and column while minimizing both the seatbelt forces applied to the driver's body and the forward rotation of the driver's head. The efficacy of a controlled seatbelt force is further increased by obtaining advanced warning of an impending collision via the magnetic sensors described in the first part of this report. The lead time gained through early crash prediction can be used both to **a)** overcome time delays associated with fully activating the restraint system and **b)** to bring the driver to a more favorable initial state prior to the start of the collision. This approach to driver restraint offers significant improvements over a simple locking elastic seatbelt.

4.4.1 Proposed Control Law

A simple control law is proposed to show the benefits of imminent collision detection compared to using a regular seat belt with pre-tightening. The proposed control law is as follows:

$$F_{pelvis} = \begin{cases} F_{p,tilt} & \text{Before actual collision, after detection of imminent collision} \\ F_{p,high} & \dot{x}_p > \varepsilon_{p,2} \\ F_{p,low} & \dot{x}_p < \varepsilon_{\mathrm{p},1} \end{cases} \tag{4.50}$$

$$F_{torso} = \begin{cases} F_{t,tilt} & \text{Before actual collision, after detection of imminent collision} \\ F_{t,high} & \dot{x}_t > \varepsilon_{t,2} \\ F_{t,low} & \dot{x}_t < \varepsilon_{t,1} \end{cases} \tag{4.51}$$

The hysteresis used in switching between forces F_{high} and F_{low} in the velocity region around $\dot{x}_p = 0$ is shown in Figure 4.4.

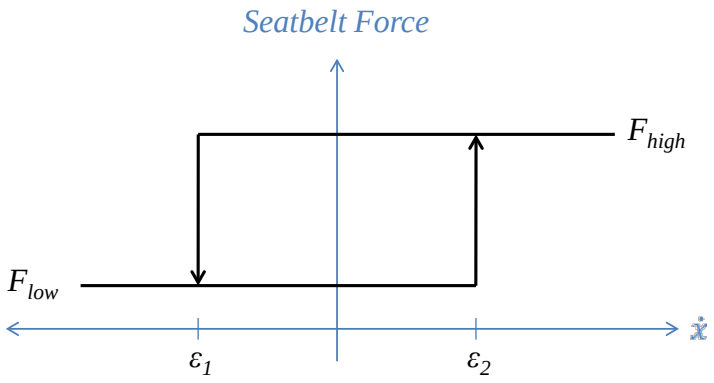

Figure 4.4: Seatbelt force hysteresis

The proposed control strategy uses a predetermined constant seatbelt tension during the occupants motion towards the steering column to absorb the driver's forward kinetic energy prior to colliding with the steering wheel and column. Since this force value is calculated before the time of collision, it is less computationally intensive than a control strategy based on real-time force calculation. When the driver's velocity relative to the car reaches a value near zero, the restraining force is reduced to a lower value adequate to support just the driver's weight. To prevent rapid switching between the higher force and the lower force, a velocity-based hysteresis is implemented. This is effective in reducing the forward rotation of the driver's head and eliminates backlash of the driver's body after the collision is over. The proposed control law is given in equations (4.50) and (4.51), and the seatbelt force hysteresis is illustrated in Figure 4.4. The algorithm used to implement the proposed controller is illustrated in the flow chart found in Figure 4.5. This algorithm is iterated repeatedly throughout the collision event. The decision processes used to determine the force value to apply to the shoulder belt and to the lap belt are functionally identical, though the specific values used for each belt are different in general. The controller uses only occupant velocity as feedback to regulate the force applied to the driver. Since this is the only measurement required, this control strategy is practical to implement.

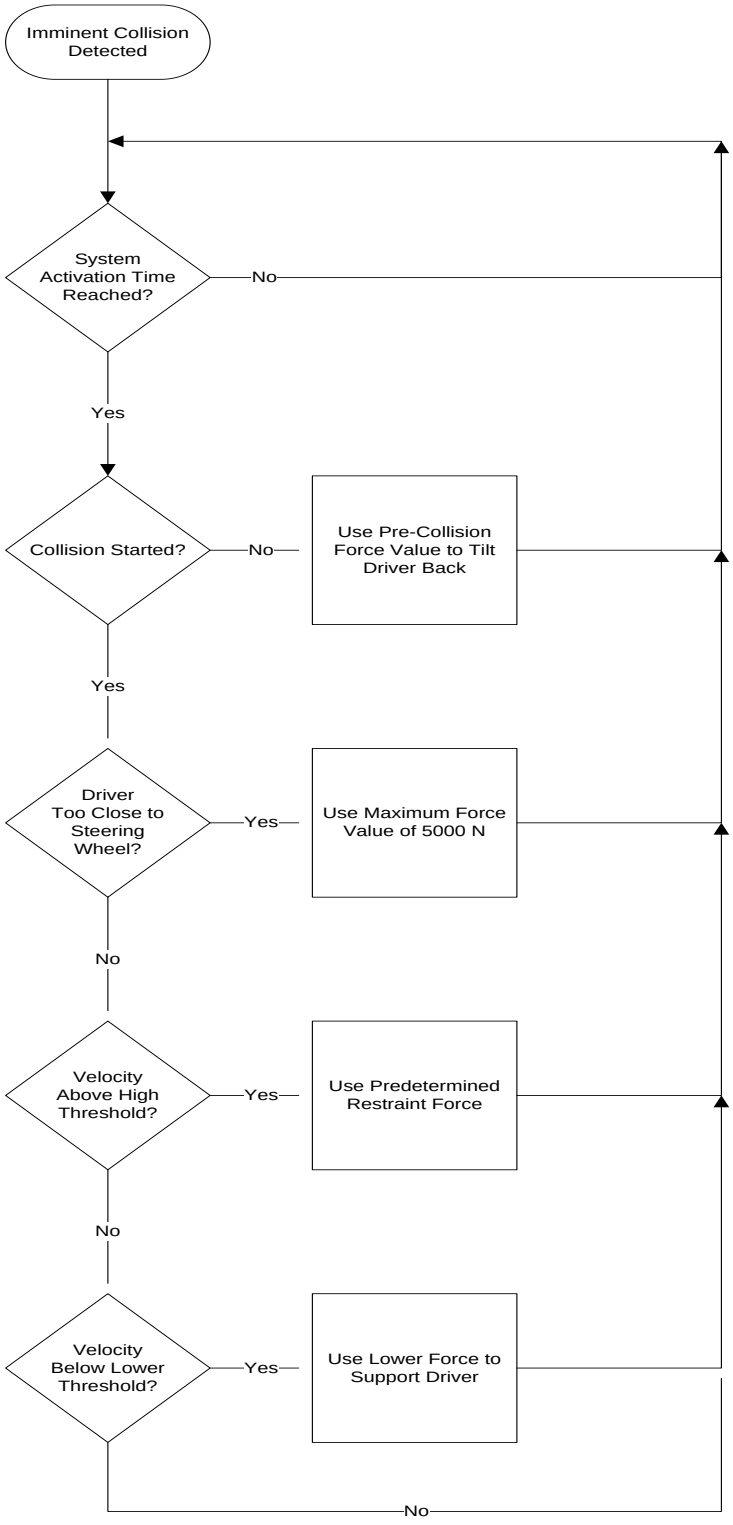

Figure 4.5: Proposed control strategy algorithm

An important component of the proposed controller is early detection of an impending collision. One significant advantage of advanced warning time is the ability to initiate the seatbelt control

system early enough to overcome time delays in the full activation of the system. Another important advantage is the ability to bring the driver's body to an initial state before collision that is more favorable for avoiding injury. The most desirable initial state with which the driver can enter the collision is one which provides the greatest possible distance to the steering wheel and the lowest possible initial velocity. Minimizing the driver's initial velocity minimizes the kinetic energy that must be overcome by the seatbelt force. Since the amount of work needed to overcome the kinetic energy is related to the product of force and distance, maximizing distance to the steering wheel effectively minimizes the required seatbelt force. This extra distance and lower inertial velocity are achieved by rotating the back of the seat away from the steering wheel while applying enough seatbelt tension to tilt the driver's torso back.

The figures below compare outcomes of a simulated 35 mph collision using the fixed elastic seatbelt model and using the proposed control strategy. Figure 4.6 shows a model of the vehicle's acceleration profile due to the collision [19], [20]. Figures 4.7 and 4.8 show the trajectory of the driver's body as the collision progresses. In Figure 4.7 we see that the fixed elastic seatbelt allows the driver's head and torso to extend past the steering wheel, likely resulting in severe injury to the driver. In Figure 4.8, on the other hand, we see that the proposed controller stops the driver just before colliding with the steering wheel. Note also that before moving forward relative to the seat, the driver in Figure 4.8 is pulled backward in order to maximize distance to the steering wheel and minimize initial velocity. These plots indicate that the likelihood of driver injury is lowered with the proposed control strategy simply because the driver does not collide with the steering wheel.

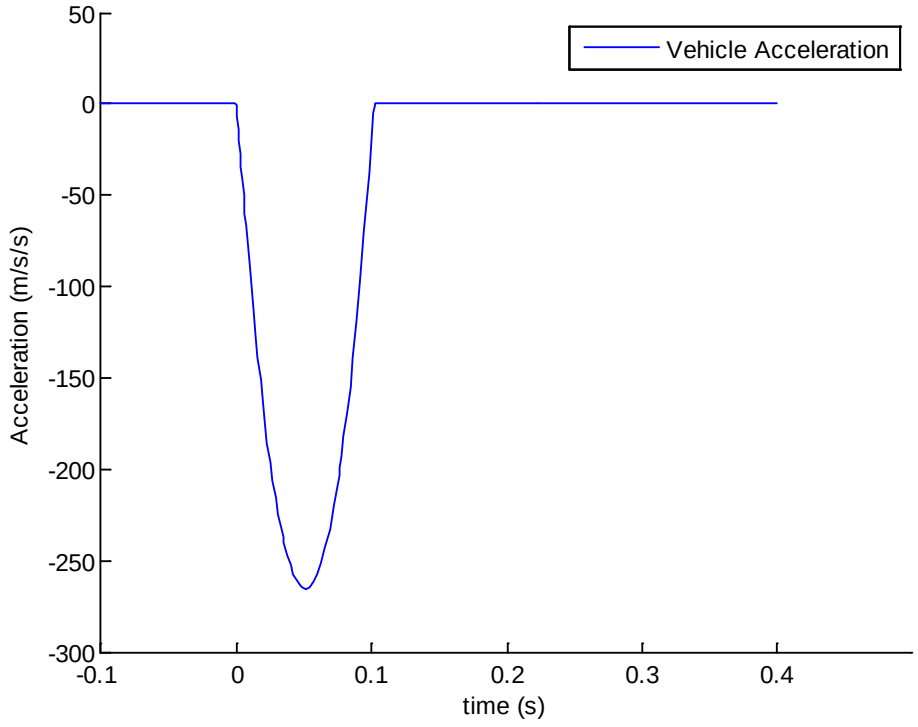

Figure 4.6: Acceleration profile of vehicle

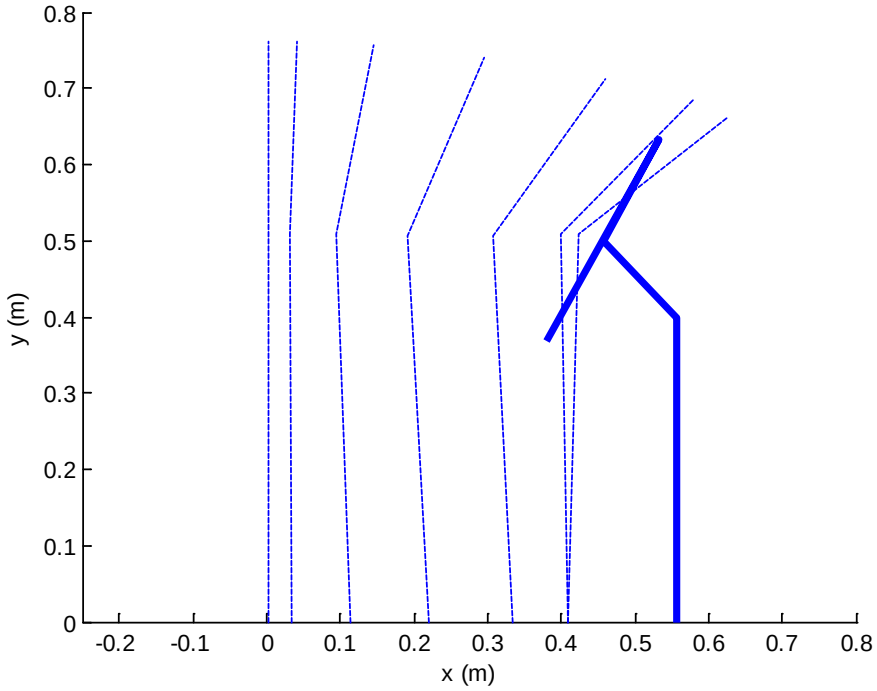

Figure 4.7: Body trajectory during a collision using fixed elastic seatbelt model

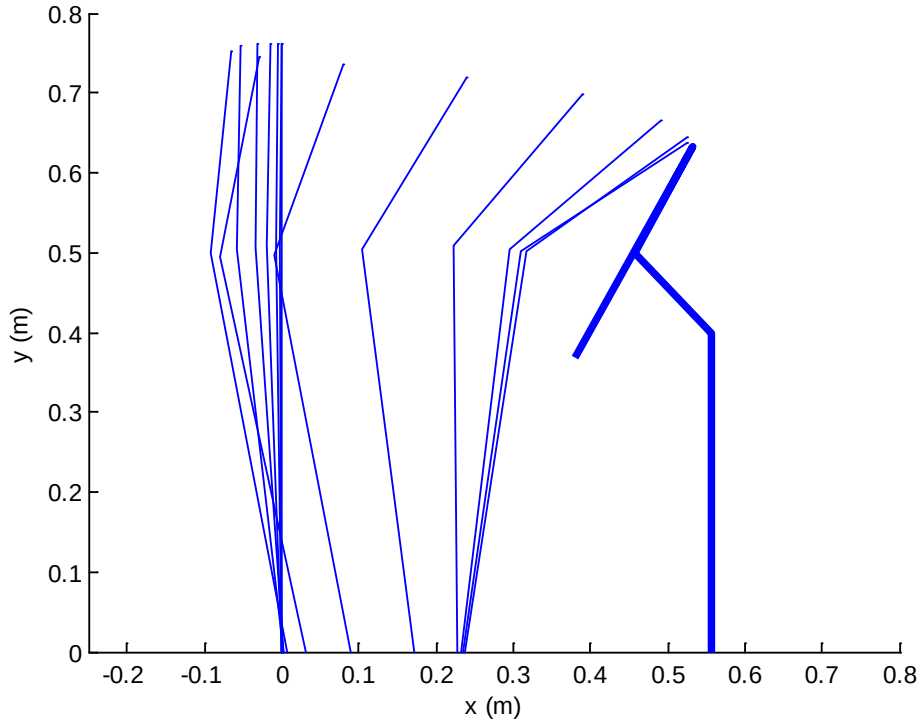

Figure 4.8: Body trajectory during a collision using proposed control strategy

Figures 4.9 and 4.10 compare the forces imparted by the seatbelt on the driver's torso and the driver's pelvis, respectively. The collision begins at time t=0.000 seconds and ends at time t=0.102 seconds. Note that both seatbelt models only begin to provide force after a lag time of 15 ms. In the case of the fixed elastic seatbelt, this delay prevents the seatbelt from providing force in the actual duration of the collision. In the case of the proposed controller, this time lag is overcome long before the collision begins due to advanced collision detection. In the case of both the torso and the shoulder, the maximum force required to stop the driver is lower using the proposed controller compared to the regular elastic seat belt.

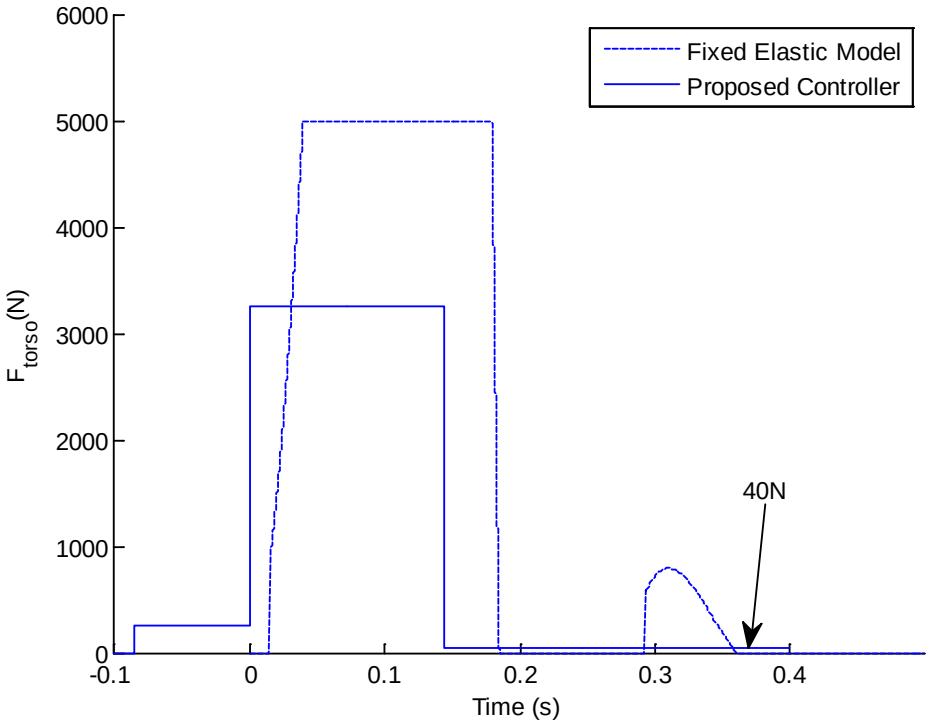

Figure 4.9: Seatbelt forces on torso during collision

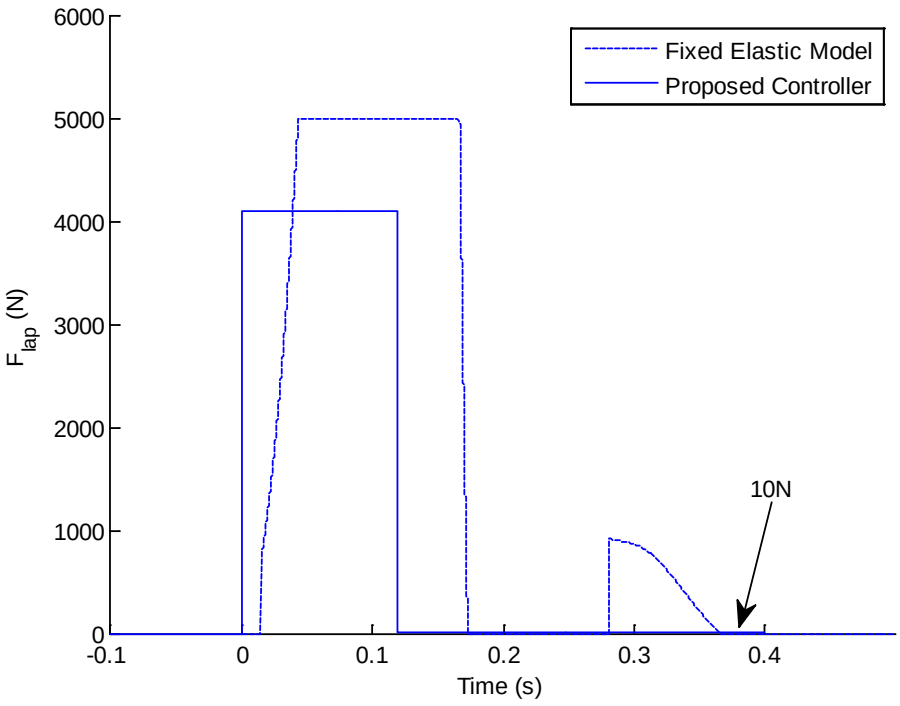

Figure 4.10: Seatbelt forces on pelvis during collision

Figure 4.11 compares the rotation of the driver's head for each seatbelt model during the collision. The maximum head rotation resulting from the proposed control strategy is nearly fifteen degrees lower than that provided by the fixed elastic seatbelt. The head rotation curve is also smoother, which is generally indicative of lower angular acceleration during the collision. The driver's risk of injury due to neck lash is thus reduced using the proposed controller.

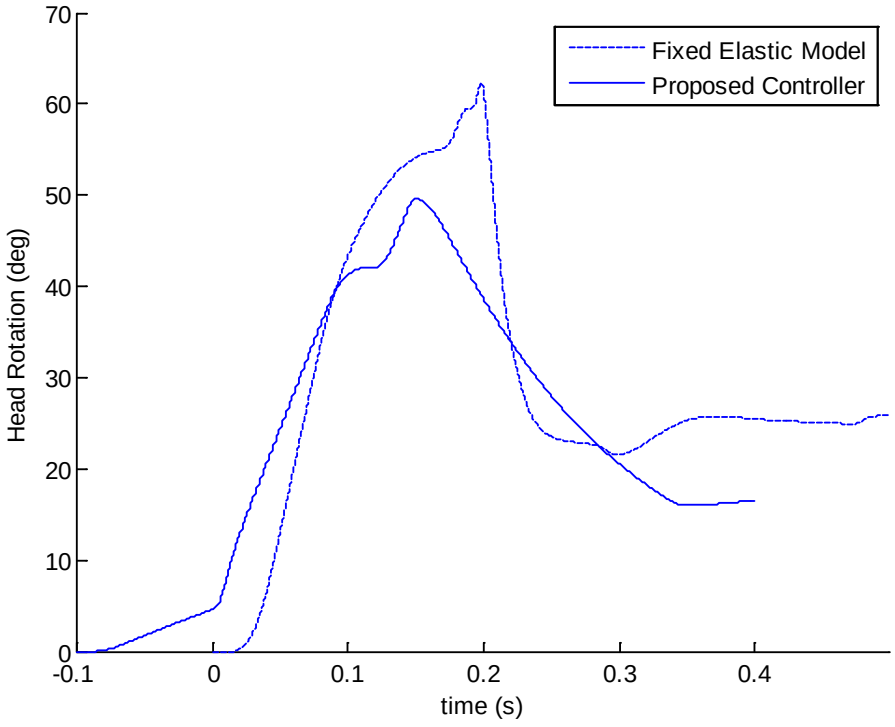

Figure 4.11: Forward rotation of head during collision

Figures 4.12-4.15 compare outcomes of the collision using the proposed controller and a second controller which does not tilt the seat back; both controllers use advanced collision detection to pretighten the seatbelts. Figure 4.12 shows the trajectory of the driver's body as the collision progresses when the controller without seat tilt-back is used. We see in Figure 4.13 that the maximum torso force required to stop the driver from colliding with the steering wheel is significantly lower for the proposed controller than that required by the controller that does not tilt the seat back. Figure 4.14 shows that there is no significant difference between the two systems in the seatbelt force applied to the pelvis. In Figure 4.15 we see that the maximum head rotation given by the second controller is about equal to that given by the proposed controller, indicating that there is very little unfavorable trade-off associated with using the proposed controller to reduce the force applied to the driver's body.

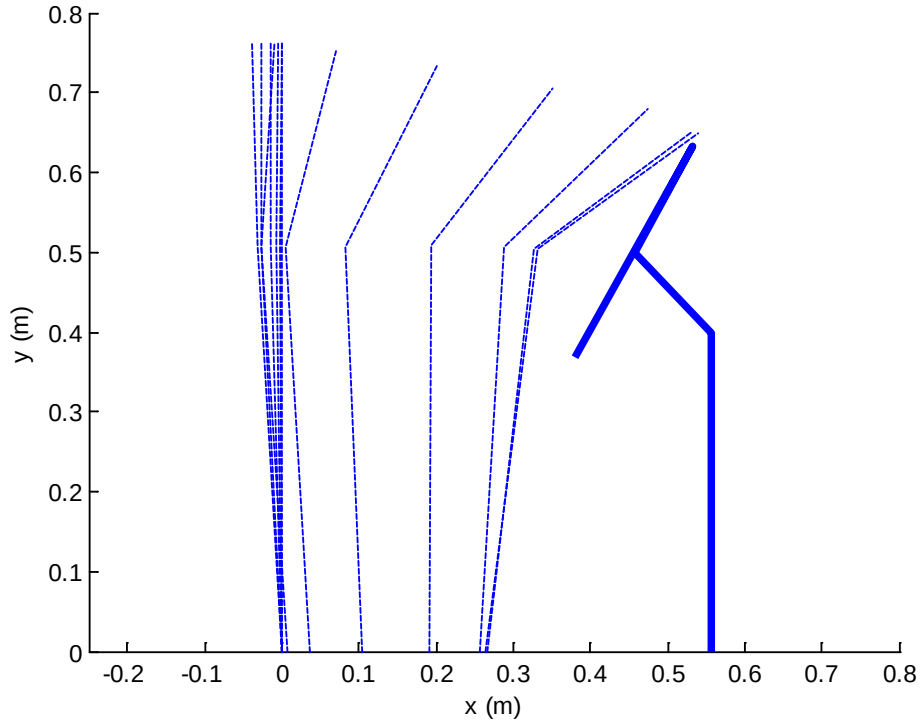

Figure 4.12: Body trajectory during a collision using only pretightening

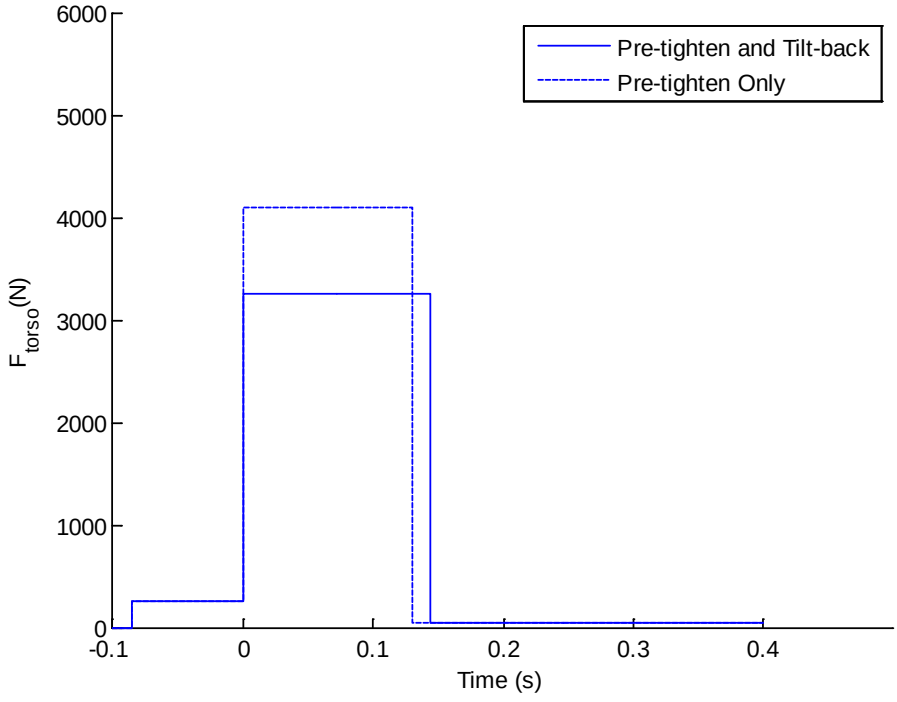

Figure 4.13: Seatbelt forces on torso during collision

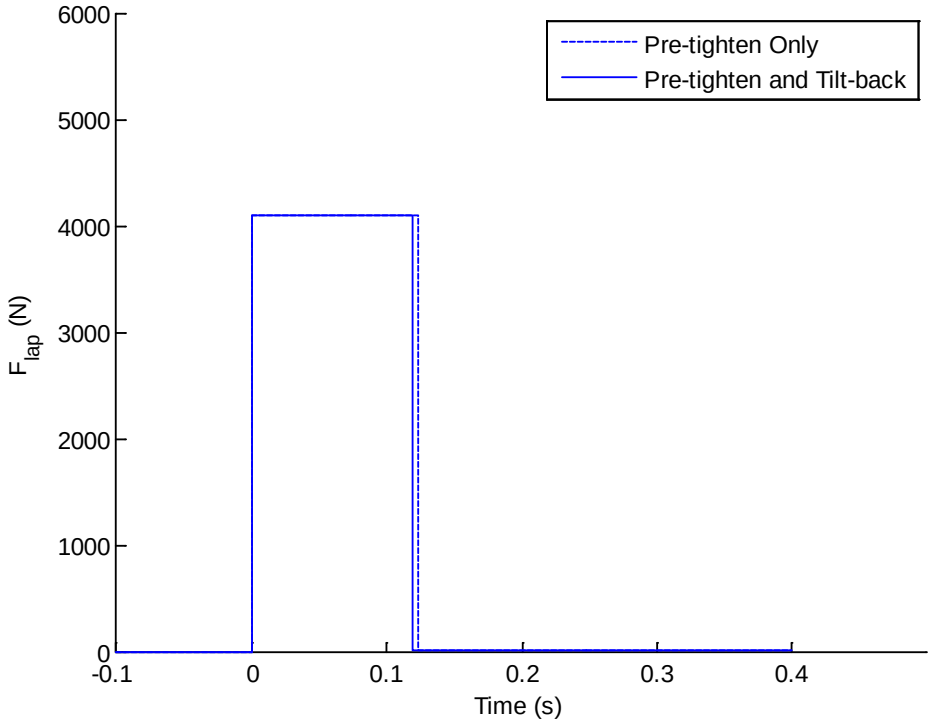

Figure 4.14: Seatbelt forces on pelvis during collision

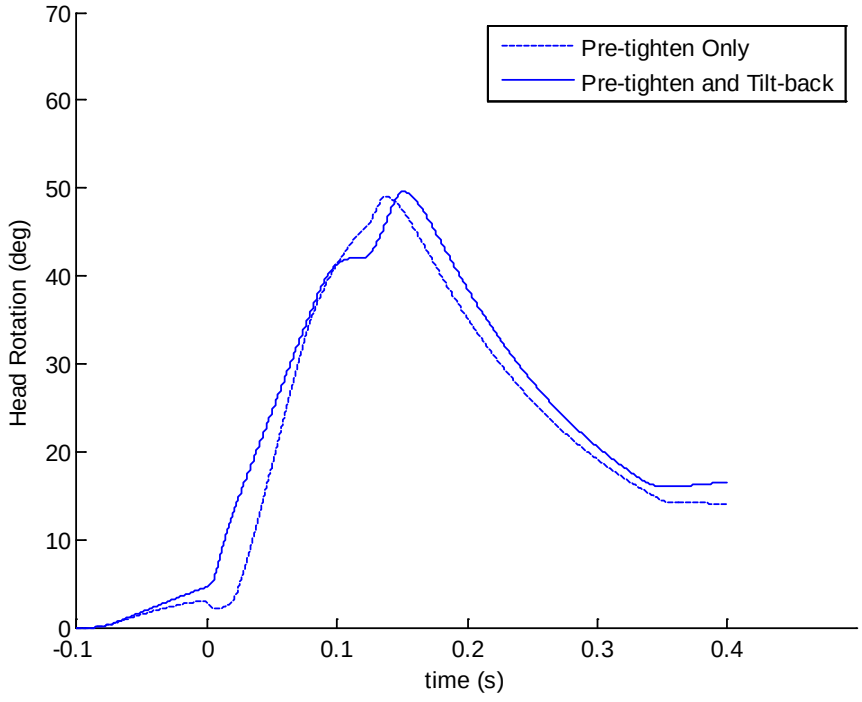

Figure 4.15: Forward rotation of head during collision

Figures 4.16 and 4.17 compare outcomes of the collision using the proposed controller and a second controller which does not use the backlash prevention scheme of reducing the seatbelt force when the velocity of the driver nears zero: the force given by the second controller is tuned to a maximum value and is left never reduced. Figure 4.16 shows the trajectory of the driver's body as the collision progresses when the controller without backlash prevention is used. In this figure, we clearly see that the driver's head extends past the steering wheel, likely causing injury. In Figure 4.17 we see that the maximum head rotation given by the second controller is much higher than that given by the proposed controller. This demonstrates the necessity of the backlash prevention shceme in the proposed control strategy.

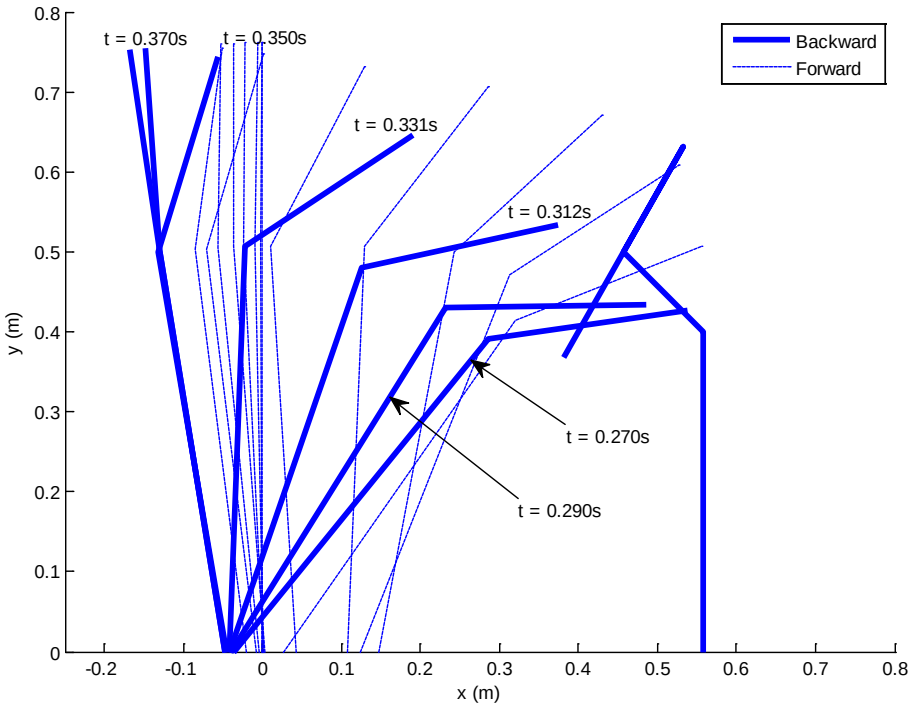

Figure 4.16: Body trajectory during a collision – without backlash prevention

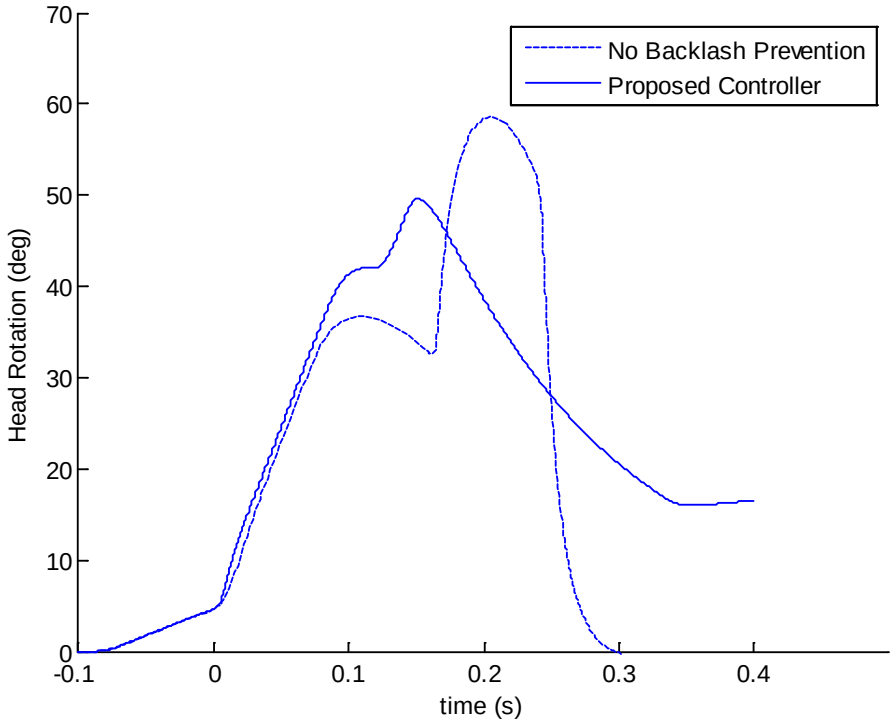

Figure 4.17: Forward rotation of head during a collision – with and without backlash prevention

5 Conclusions

This project focuses on the development of a novel and unique automotive sensor system for the measurement of relative position of another vehicle in close proximity. The sensor system was based on the use of anisotropic magnetoresistive (AMR) sensors which measure magnetic field. While AMR sensors have previously been used to measure traffic flow rate and to detect vehicles in parking spots, they have never before been used to measure the relative position of the vehicle.

Analytical formulations were developed to predict the relationships between position and magnetic field for both one-dimensional and two-dimensional relative motion. The use of these relationships to estimate vehicle position is complicated by the fact that the parameters in the relationship vary with the type of vehicle under consideration. Since the type of vehicle encountered is not known apriori, the parameters for the magnetic field-position relationship have to be adaptively estimated in real time.

A system based on the use of multiple AMR sensors together with an iterated adaptive Kalman filter was developed to estimate vehicle parameters and position. The use of additional sonar sensors helps improve speed of convergence of the algorithm. Test results with a wheeled laboratory test rig consisting of a door and tests with several full scale passenger sedans were presented. The experimental results in this report confirm that the developed sensor system is viable and that it is feasible to adaptively estimate vehicle position even without knowledge of vehicle-dependent parameters.

In order to demonstrate the value of the developed sensor system in enhancing occupant safety during a crash, simulation results on occupant motion during a frontal crash were presented. First, a dynamic model for occupant motion inside the car during a front-to-back crash was developed using a Lagrangian formulation. Then control laws with and without prediction of an imminent collision were developed and implemented in simulation. The simulations demonstrated that knowledge of an imminent crash, 100 milli-seconds before the crash occurs, could significantly enhance the safety of the occupant and prevent his/her collision with the steering column while simultaneously minimizing the seat belt forces that act on the occupant.

References

[1] M. Pannetier-Lecoeur, L. Parkkonen, N. Sergeeva-Chollet, H. Polovy, C. Fermon and C. Fowley, "Magnetocardiography with sensors based on giant magnetoresistance," *Applied Physics Letters*, 98, 153705 (2011).

[2] R. Macedo, F.A. Cardoso, S. Cardoso, P.P. Freitas, J. Germano and M.S. Piedade, "Self-Powered Hybrid Antenna-Magnetoresistive Sensor for Magnetic Field Detection," *Applied Physics Letters*, 98, 103503 (2011).

[3] J. Loureiro, R. Ferreira, S. Cardoso, P.P. Feritas, J. Germano, C. Fermon, G. Arrias, M. Pannetier-Lecoeur, F. Rivadulla and J. Rivas, "Toward a Magnetoresistive Chip Cytometer: Integrated Detection of Magnetic Beads Flowing at cm/s Velocities in Microfluidic Channels," *Applied Physics Letters*, 95, 034104 (2009).

[4] S.B. Patil, A. Guedes, P.P. Freitas, S. Cardoso, V. Chu and J.P. Conde, "On-Chip Magnetoresistive Detection of Resonance in Microcantilevers," *Applied Physics Letters*, 95, 023502 (2009).

[5] C. Albon, A. Weddemann, A. Auge, K. Rott and A. Hutten, "Tunneling Magnetoresistance Sensors for High Resolutive Particle Detection," *Applied Physics Letters*, 95, 023101 (2009).

[6] M.H. Kang, B.W. Choi, K. C. Koh, J.H. Lees, and G.T. Park, “Experimental study of a vehicle detector with an AMR sensor,” *Sensors and Actuators, A: Physical*, 118(2), 278-284 (2005).

[7] J. Vcelak, P. Ripka, J. Kubik, A. Platil and P. Kaspar, "AMR Navigation Systems and Methods of Their Calibration," *Sensors and Actuators A: Physical*, 123-124, 122-128 (2005).

[8] H. Knoepfel, *Magnetic Fields: A Comprehensive Theoretical Treatise for Practical Use.* Hoboken, NJ: Wiley (2000).

[9] D.J. Griffiths, *Introduction to Electrodynamics*. Upper Saddle River, NJ: Prentice Hall (1999).

[10] Y. Bar-Shalom, X. Rong Li and T. Kirubarajan, *Estimation with Applications to Tracking and Navigation.* Hoboken, NJ: Wiley (2001).

[11] D. Simon, *Optimal State Estimation: Kalman, H Infinity, and Nonlinear Approaches.* Hoboken, NJ: Wiley (2006).

[12] S. Julier, J. Uhlmann and H.F. Durrant-Whyte, "A new method for the nonlinear transformation of means and covariances in filters and estimators," *IEEE Transactions on Automatic Control,* 45, 477-482 (2000).

[13] T. Lefebvre, H. Bruyninckx and J. De Schuller, "Comment on 'A new method for the nonlinear transformation of means and covariances in filters and estimators' [and authors' reply]," *IEEE Transactions on Automatic Control,* 47, 1406-1409 (2002).

[14] R. Mobus and U. Kolbe, "Multi-target multi-object tracking, sensor fusion of radar and infrared," *IEEE Intelligent Vehicles Symposium*, Parma, Italy, 732 – 737 (2004).

[15] S. Matzka and R. Altendorfer, "A Comparison of Track-to-Track Fusion Algorithms for Automotive Sensor Fusion," *Proceedings of IEEE International Conference on Multisensor Fusion and Integration for Intelligent Systems*, Seoul, Korea, August 20-22 (2008).

[16] G.R. Widmann, M.K. Daniels, L. Hamilton, L. Humm, B. Riley, J.K. Schiffmann, D.E. Schnelker and W.H. Wishon, *Comparison of Lidar-Based and Radar-Based Adaptive Cruise Control Systems*. Troy, MI: Delphi Automotive Systems Report, 2000-01-0345.

[17] M.I. Ki, K. Yi, D. Caveney and J.K. Hedrick, "A multi-target tracking algorithm for application to adaptive cruise control," *Journal of Mechanical Science and Technology*, 19(9), 1742-1752 (2005).

[18] D. Caveney, B. Feldman and J.K. Hedrick, "Comprehensive Framework for Multisensor Multi-target Tracking in the Adaptive Cruise Control Environment," *Proceedings of the 6th International Symposium on Advanced Vehicle Control (AVEC)*, Hiroshima, Japan, September,697-702 (2002).

[19] T.J. Paulitz, D.M. Blackketter and K.K. Rink, "Fully-adaptive seatbelts for frontal collisions," *Proceedings of the 19th International Technical Conference on the Enhanced Safety of Vehicles (ESV)*, Washington, D.C., June (2005).

[20] T.J. Paulitz, "Adaptive Seatbelt Restraints for Frontal Collisions," M.S. Thesis, Moscow, ID: University of Idaho, Department of Mechanical Engineering, December (2004).